UiO : Department of Geosciences
University of Oslo

The vertical structure of currents in Arctic and sub-Arctic regions

Karen Augusta Jarstø Ervik

Master's Thesis, Spring 2022

Abstract

Motivated by previous research on currents vertical structure worldwide, this study aims to analyze the Arctic Ocean's vertical structure further. The Arctic is highly susceptible to climate changes and is experiencing the fastest environmental changes in the world in response to Arctic amplification. Warming of the atmosphere and terrestrial environment in the Arctic contributes to sea-ice melt and ocean warming, resulting in altered circulation dynamics as the ocean becomes warmer and fresher. Therefore, understanding the deep ocean's vertical structure is vital to comprehending the complexity of the ocean currents' heat transport and transport of other properties.

In this study nineteen empirical orthogonal functions (EOF) derived from mooring records deployed in the Arctic and sub-Arctic region are analyzed to characterize the ocean's vertical structure in higher latitudes. The EOFs are orthogonal basis vectors in the principal direction of the data set's variability. Thus, the primary vertical EOF demonstrates the dominant variability with depth. The mooring records are further rotated along the principal direction of the horizontal variability (the horizontal EOF1 and EOF2) at the mooring location to explore the degree of topographic steering. Because the mooring records contain missing values, which are substituted with zero, the EOFs may be misguided for levels missing data. The solution has been to derive the total variance estimated with depth, constructed by removing the missing values, to assess the validity of the EOFs.

The EOFs revealed subsurface maximum and non-vanishing velocity at the lower measurements. However, all the EOFs declined with depth, and only one EOF exhibited zero crossing. Thus the first 'rough bottom' baroclinic mode represents the EOFs best. Furthermore, seventeen records demonstrated a sharp increase from the first measurement, depicted by the EOFs and confirmed by the calculated total variance. The two remaining EOFs revealed the same tendency. However, the total variance denies the increase for these stations. As most of the moorings are deployed on the continental slope, a greater fraction than anticipated demonstrated isotropic variance.

In addition to the mooring records, a numerical ocean model is utilized to expand the locations investigated. The model EOFs were chosen to explore additional effects of sea ice cover and flat and sloping bottom characteristics on the vertical structure. However, the model displayed poor reliability in reproducing the vertical structure at the observation site.

In conclusion, the findings in this study were unexpected. Further investigation of the deep ocean's vertical structure is required, along with improved ocean modeling at higher latitudes.

Abstract

Norwegian Abstract

Motivert av tidligere forskning på den vertikale struktur til havstrømmene over hele kloden, ønsker denne studien å analysere polhavets vertikale struktur. Arktis er svært utsatt for klimaendringer og gjennomgår de raskeste miljøendringene i verden som følge av 'Arktisk forsterkning'. Oppvarming av atmosfæren og det terrestriske miljøet i Arktis bidrar til havissmelting, bresmelting og oppvarming av havene, som igjen resulterer i endret sirkulasjonsdynamikk etter hvert som havet blir varmere og ferskere. Kunnskapen om dyphavets vertikale struktur er derfor avgjørende for å forstå kompleksiteten i havstrømmenes transport av varme og andre egenskaper.

Nitten empiriske ortogonale funksjoner (EOF) utledet fra moringer stasjonert i arktiske og subarktiske regionen er analysert for å karakterisere havets vertikale struktur ved høyre breddegrader. EOFer er ortogonale basisvektorer i hovedretningen til datasettets variabilitet. Dermed demonstrerer den primære vertikale EOF den dominerende variasjonen med dybden. Videre roteres hastighetsverdiene fra moring-dataen langs hovedretningen til den horisontale variansen (fra horisontale EOF1 og EOF2) ved moring lokasjonen for å utforske graden av topografisk styring på strømmene. Fordi moringdataen inneholder manglende verdier, som erstattes med null, kan EOF-ene være feilorientert for disse nivåene. Løsningen har vært å utlede den totale variansen estimert med dybden, konstruert ved å fjerne de manglende verdiene. Den totale variansen er utledet for å validere påliteligheten til EOF-ene.

EOF-ene viser maksimal varians nedenfor overflatelaget, samt ikke-forsvinnende hastighet ved den nederste målingen. Alle avtar i styrke med dyp, og bare en EOF demonstrerte nullkryssning. Dermed representerer den første barokliniske 'ruglete-bunn' modusen EOF-ene best. Videre viste sytten målestasjoner en kraftig økning fra den første målingen avbildet av EOF-ene og er bekreftet av den totale variansen. De to gjenværende EOF-ene viste også den samme tendensen, men for disse målestasjonene avviset den totale variansen økningen. Ettersom de fleste av moringene er utplassert på kontinentalskråningen, viste flere enn forventet isotrop varians.

I tillegg til moringene brukes en numerisk havmodell for å utvide studiens geografisk omfang. EOF-ene utledet fra modelldataen er valgt for å utforske ytterligere effekter av havisdekke, samt flat og skrånende havbunn på den vertikale strukturen. Modellen viste seg imidlertid dårlig egnet til å gjengi den vertikale strukturen på observasjonsstedet.

Funnene i denne studien var uventede. Ytterligere undersøkelser av dyphavets vertikale struktur er nødvendig, sammen med forbedret havmodellering på høyre breddegrader.

Acknowledgements

First and foremost, I would like to thank my supervisors, Joseph H. LaCasce and Pål Erik Isachsen, for their excellent guidance and for making this thesis possible. The project has been both challenging and rewarding.

Thanks to Camille Lique and Claude Talandier at IFREMER for providing me with the model simulations from CREG12.

A huge thanks to Anna Fouilloux for helping me with all my technical problems and endless questions. Thank you for providing me access to Galaxy Live so I could complete my results. It has been an enormous help.

To the reading spot - What a tremendous group with excellent people. I would never have finished these two years without you. Thanks for the love and support, the patience and laughter we have shared. And a special thanks to Anna Lina for every time I borrowed her brain. It is brilliant!

Thanks to dad for the daring attempt to improve my writing and to mom for the endless support.

Karen Augusta Jarstø Ervik
May 2022
Oslo.

Contents

Abstract i

Abstract iii

Acknowledgements v

Contents vii

List of Figures ix

List of Tables xi

1 Introduction 1
- 1.1 Motivation . . . 1
- 1.2 Study area . . . 3
- 1.3 Research questions . . . 4
- 1.4 Outline . . . 5

2 Theory 7
- 2.1 Quasi-geostrophic framework . . . 7
- 2.2 Baroclinic flow . . . 7
- 2.3 Topographic waves . . . 12

3 Observations, model and methods 13
- 3.1 Current meter records . . . 13
- 3.2 The numerical ocean model; CREG12.L75 . . . 15
- 3.3 Principal Component Analysis/Empirical Orthogonal Functions . . . 16

4 Results 19
- 4.1 An overview of the flow field and its variability. . . . 20
- 4.2 Vertical structures at observation sites. . . . 28
- 4.3 The role of sea ice . . . 35

5 Discussion and Conclusion 43
- 5.1 Interpretations in terms of baroclinic modes . . . 44
- 5.2 Further research . . . 47
- 5.3 Conclusion . . . 48

Appendices 49

A Figures and Tables 51
- A.1 Figures . . . 51

A.2 Tables 51

B Computer Code **53**

C Equations **55**
C.1 β-approximation 55
C.2 QG-Density equation 55

Bibliography **57**

List of Figures

1.1 A topographic map of the Arctic ocean basin 4

3.1 Map over the Arctic and sub-Arctic region, with mooring location. 14

4.1 Time averaged velocity at 35 meters depth. 21
4.2 Time averaged velocity at 333 meters depth. 22
4.3 Time averaged velocity for the bottom currents. 23
4.4 Horizontal variance ellipses for the current at 35 meters depth. 24
4.5 Horizontal variance ellipses for the current at 35 meters depth in the Norwegian Sea. . 25
4.6 Horizontal variance ellipses for the currents at 333 meters depth. 26
4.7 Horizontal variance ellipses for the currents at 333 meters depth in the Norwegian Sea. 27
4.8 Horizontal variance ellipses for the bottom currents. 28
4.9 Horizontal variation ellipses derived from observation records. 29
4.10 Horizontal variation ellipses derived from model data at observation site. 30
4.11 EOF1 and EOF2 derived from observation data in Lofoten. 31
4.12 EOF1 and EOF2 derived from observation data North of Svalbard. 32
4.13 EOF1 and the total variance with depth derived from model and observation data North of Svalbard, East 33
4.14 EOF1 and the total variance with depth derived from model and observation data North of Svalbard, West 34
4.15 Practical salinity and derived potential density obtained from observation records located North of Svalbard. 35
4.16 EOF1 and the total variance with depth derived from model and observation data in Lofoten 36
4.17 Practical salinity and derived potential density obtained from observation records located in Lofoten. 36
4.18 EOF1 and the total variance with depth derived from model and observation data on Yermak Plateau. 37
4.19 Practical salinity and derived potential density obtained from observation records located on Yermak Plateau. 38
4.20 Map of sea ice cover and ice thickness from model. 39
4.21 EOF1 and the total variance with depth derived from model over ice free regions. . . . 40
4.22 EOF1 and the total variance with depth derived from model in ice covered regions over steep terrain. 40
4.23 EOF1 and the total variance with depth derived from model ice covered region over flat or rough terrain. 41

A.1 EOF1 and the total variance with depth derived from model and observation data obtained from the Beaufort Sea. 51
A.2 EOF1 and the total variance with depth derived from model and observation data obtained from the Barents Sea. 52

List of Tables

3.1 Details of Mooring Deployments 18

CHAPTER 1

Introduction

1.1 Motivation

The satellite survey was a significant breakthrough for ocean science, providing a much-needed overview of the surface current to a global extent. Today, almost simultaneous satellite data present a 1/4 ° grid map of sea surface height (SSH) and surface salinity worldwide, along with a 1 km grid map for the surface temperature. However, understanding how these surface fields reflect in the interior is still uncertain. Understanding the deep ocean's vertical structure is vital to comprehending the complexity of the ocean currents' heat transport and transport of other properties.

Several studies aim to reconstruct internal flow fields, providing various techniques to project the vertical structure of the interior ocean. De Mey and Robinson (1987) proposed to use empirical orthogonal functions (EOFs), commonly known as a Principal Component Analysis (PCA) in statistics, to capture the largest variability of the vertical structure in the interior. EOF-analysis is a technique to reduce the dimensions of large data sets while preserving most of the information. Each EOF is a new variable constructed as a linear combination of the original variables, yielding a set of orthogonal basis functions. The first component, EOF1, contains the largest fraction of the information from the data set, followed by the second component, containing the second-largest fraction of information orthogonal to the first component, and so forth, upon which the data can be projected. The percent of variance explained (PVE) reflects how much variance each EOF represents. Thus, for one or two EOFs dominating the PVE, the credibility of the analysis is strengthens. However, the disadvantage of using this approach to determine vertical structure is that it necessitates a large number of observations worldwide.

Obtaining substantial observation data for the ocean is challenging as the ocean is a remote region. Wunsch, 1997 proposed a vertical extension of his and Stammer's (Wunsch and Stammer, 1995) estimation of the space and time spectra of global variability for the sea surface height and slope obtained from altimeter records. This offered a preferred approach for estimating the vertical structure by utilizing climatology data from satellite surveys on predefined analytical structures such as the baroclinic (BC) and barotropic (BT) modes. The horizontal surface velocities are derived from the SSH measurements, assuming 'Quasi-geostrophic balance' and vanishing density gradient at the surface. The calculated velocities are further projected into the interior on the modes. According to Wunsch's findings, the BT and BC1 modes account for 90% of the variance. However, the BC mode revealed a more substantial surface imprint in the SSH, whereas the BT mode shows little or no skill in capturing the SSH. Wunsch suggests that SSH-anomalies primary reflects the motion of the main thermocline, hence the BC1-mode (Wunsch, 1997). Variability in SSH can be decomposed into BT and BC contributions, where the BT contribution comes from net mass changes in the water column. In contrast, the BC contribution comes from changes in density connected to sloping density surfaces over ocean currents (Baker-Yeboah et al., 2009). Furthermore, Wunsch estimated EOFs from altimeter records, which revealed a vertical structure resembling a combination of the BT and BC1 modes. Stammer, 1997 found the same year results consistent

with Wunsch, showing that the length scale of SSH anomalies often are proportional to the BC1 mode. However, although Wunsch and Stammer found the SSH to capture the BC1 signal better, the BT mode is equally important with depth. Thus, by using the SSH measurements approach, only half the vertical structure is captured without more information about the BT mode.

A new approach based on 'surface-quasi-geostrophy' (SQG) (Held et al., 1995) was developed in 2006 by several different studies (LaCasce and Mahadevan, 2006, Lapeyre and Klein, 2006, Isern-Fontanet et al., 2006 and Tulloch and Smith, 2006) to address the issues of the BT mode and SSH measurement. SQG uses a more dynamical approach for subsurface field estimation, attempting to connect horizontal and vertical motion scales. SQG is appealing as it uses a more two-dimensional method, creating potential vorticity (PV) fields, derived from the sea surface temperature (SST) and inverted to get the pressure in the vertical (LaCasce and Mahadevan, 2006). The SST has a higher spatial resolution than the SSH, thus it may depict the vertical structure more accurately. The method showed remarkable resemblance down to a few hundred meters. However, the structure became consistently too weak at greater depths.

Several approaches to connect the BC/BT mode and SQG is explored. Lapeyre, 2009, for example, proposed a technique appending an SQG component onto the BC mode to compensate for the vanishing density gradient at the surface. However, this approach imposed a problem as the SQG solution is not orthogonal to the BC1. Therefore, Wang et al., 2013 extended this' approach by calculating the two modes separately by supplementing an amplitude fitting the SSH pressure after subtracting SQG-contribution onto the BT and BC modes. The approach combines SQG-approximation for the surface density with interior-QG, assuming residual anomalies in SSH reflect the PV in the interior. The reconstruction was successful for the velocity and density down to 1000 meters. However, the method requires surface density, calculated using SST as a proxy. Therefore, it is a good approximation in regions where SST dominates the density but will have problems where sea surface salinity is more important for the surface density. Furthermore, vertical profiles of the stratification, $N^2(z)$, are also required and may impose problems. Nevertheless, the method is confirmed insensitive to small changes in N. LaCasce and Wang, 2015 later simplified this approach, assuming the motion vanishes with depth and employing an exponential expression for the stratification. This method requires the climatology on a basic e-folding scale and performs efficiently compared with a subsurface field to a depth of 1000 meters. Furthermore, implementing a mixed layer improved the response in the mixed layer itself and at higher latitudes where the mixed layer is deeper. However, the mix-layer did not improve the solution in the interior and abyssal. Noticeably, the structure estimated assuming vanishing motion with depth resembles the BC1 calculated with zero horizontal flow at the boundary, referred to as a 'rough bottom' boundary condition. The BC1 calculated with the 'rough-bottom' condition complies with Wunsch, 1997 results, where the calculated EOFs obtained from observation data resembled a combination of BC1 ('flat bottom') and BT assuming the two modes cancel each other at the bottom. This would be preferable as the structure is explained solemnly in one mode rather than a combination of two.

La Lama et al., 2016 investigated this approach further by examining 81 calculated EOFs from different mooring records stationed around the globe and comparing them to baroclinic structures estimated with 'flat' and 'rough' bottom conditions. In agreement with previous results (LaCasce and Wang, 2015, and LaCasce, 2017), the investigated EOFs by La Lama et al., 2016 showed a closer resemblance to the baroclinic mode calculated 'rough bottom' than the 'flat bottom'. However, the 'rough-bottom' condition excludes the BT mode as the horizontal velocities vanish at the boundary. Thus, additional information is required on the vertical structure. For a sloping bottom, the BT mode is replaced by a topographic wave emerging from perturbations caused by changes in the seabed height. For vertical profiles demonstrating non-vanishing velocities at the bottom, the topographic wave contribution would be subtracted from the solution ahead of projecting onto the BC-mode. Nevertheless, this requires additional information about the wave, and the solution is still incomplete. Although the majority of the examined EOFs by La Lama et al., 2016 resembled the 'rough-bottom' BC1, some behaved differently. The EOFs from moorings deployed at higher latitude revealed a slower decay with depth than expected for the 'rough bottom' BC1 mode. Thus

the projection becomes less accurate. De La Lama suggested the weaker stratification in higher latitudes to be the reason for the slower decay, as the EOF and the analytical BC1 mode vary more in the abyssal, where the density becomes uniform with depth.

This thesis is an extension of La Lama et al., 2016 findings, dedicated to the Arctic region. The aim is to characterize the vertical structure of the currents in the Arctic and sub-Arctic region and identify what constrains the fluctuations. Nineteen current meter records from various research and years are studied. Each record is rotated after the two gravest EOFs estimated from horizontal velocities to investigate the impact of topographical restrictions on the current. The initial plan was to compare estimated EOFs from observation records to the baroclinic mode with 'rough' and 'flat' bottom conditions, as presented by La Lama et al., 2016. However, the Coriolis parameter becomes diminutive at higher latitude, approaching zero at 90° North. Consequently, Rossby waves horizontal scales vary significantly with latitude, becoming large at low latitudes and smaller at high latitudes. This results in Rossby waves oscillating over a long period in the Arctic, lasting over the years.

In addition to the current meter records, a numerical ocean model functioning as a model reality is utilized. The numerical ocean configuration expands the data locations to achieve data everywhere in the Arctic Ocean. Thus, a broader selection of vertical profiles can be investigated, and the desired dynamic properties selected. The EOFs are derived at the exact location as the current meter records to verify the model performance by comparing the two methods. Unfortunately, the model and the observation data employed in this thesis have too short a duration for investigating fluctuating features of planetary Rossby waves in the Arctic, as they cover a year of variations. However, lacking a theory more suited for this study, the calculated EOFs will nevertheless be interpreted in terms of baroclinic modes calculated with 'rough' and 'flat' bottom conditions.

1.2 Study area

The Arctic Ocean is a confined sea with two main passageways, the Bering Strait with cold Pacific water between Canada and Siberia, and the Fram Strait with warmer and more saline water from the Atlantic (See Fig.1.1). The ocean is divided into two main basins; the Canadian and the Eurasian basin, separated by Lomonosov Ridge. The stratification here is dominated by freezing and melting, rather than cooling and heating as in lower latitudes, due to the cold temperatures (Rudels et al., 1991) and can be divided into three distinct layers. The first is the thin surface layer, consisting of cold and fresh water due to ice melt and precipitation. This layer includes a halocline, where salinity increases rapidly with depth, separating the cold surface layer from the warmer water below (Nummelin et al., 2015). The second layer consists of warmer and saline water with Atlantic properties, whereas the last abyssal layer consists of cold and saline Arctic water.

The Arctic ocean is one of the least explored places on Earth due to its remoteness. The region is highly susceptible to climate changes and is experiencing the fastest environmental changes on the Earth in response to Arctic amplification. Warming of the atmosphere and terrestrially environment in the Arctic contributes to sea-ice melt, resulting in altered circulation dynamics as the ocean becomes warmer and fresher (Overland et al., 2019). Therefore, a quantitative examination of observation data is necessary to improve our understanding of the Arctic ocean.

In higher-latitude, the flow streams are parallel to potently vorticity contours, dominated by gradients of depths. As the variations in the Coriolis parameter are small in higher latitude, can changes in f not compensate for changes in depth, thus constraining the flow to follow the topography. The potential vorticity contours in higher latitudes thus become:

$$\bigtriangledown PV \sim \bigtriangledown \frac{f}{H} \sim f \bigtriangledown \frac{1}{H} \tag{1.1}$$

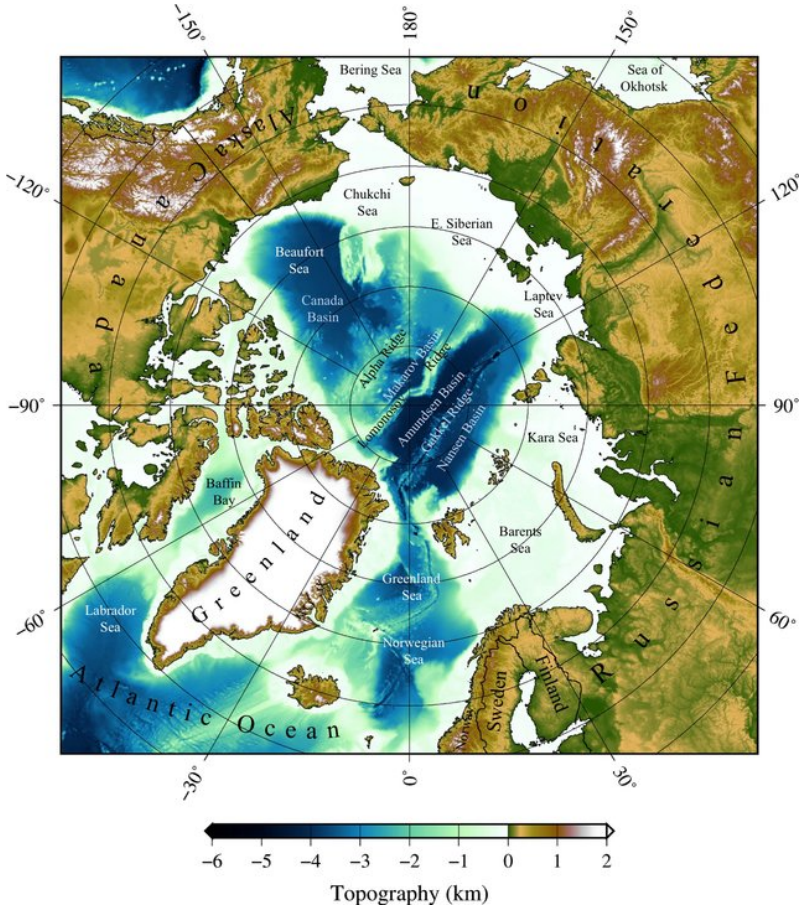

Figure 1.1: A topographic map of the Arctic ocean basin. The depth can be read from the color bar below. Source: Armitage, 2016.

In conclusion, one may expect the currents in the Arctic to be restricted by the topography, guiding the flow along the contours. Flow over steep topography, such as continental slope, can induce bottom intensified topographic waves. The sea ice may also influence the vertical structure by dampening the wave signal at the surface. Meneghello et al., 2021 found friction with the sea ice to dissipate existing eddies and prevent the growth of new ones, reducing the eddy activity in the surface layer.

1.3 Research questions

Motivated by the results presented by La Lama et al., 2016, and an urge to enhance our knowledge about the Arctic ocean, the following research questions are raised:

1. What is characterizing the vertical structure of currents fluctuations in higher latitude regions?
2. To what extent is the bottom topography affecting the structure?
3. Which analytical framework resembles the vertical structure in higher latitude regions best?
4. Suppose the structure resembles BC1 calculated with zero horizontal flow at the lower boundary, $u'(-h) = 0, \psi'(-h) = const = 0$. For that case, does the kinematic boundary condition refer most to 'steep bottom' or 'rough bottom' for flow in higher latitudes?

In order to answer the research questions, nineteen current meter records are obtained from five different mooring stations and research projects and analyzed to investigate the vertical structure of the Arctic and sub-Arctic region currents. Furthermore, as the Arctic ocean is still relatively undiscovered and few observation records exist, a numerical ocean model is employed to examine the vertical structure from a lager area in the Arctic. As sufficient theory for the vertical structure in the Arctic is still undeveloped, this study takes an empirical approach.

1.4 Outline

This thesis is structured as follows:

Chapter 2 presents the main assumption for a QG-framework, along with the derivations of the baroclinic mode calculated with 'rough' and 'flat' bottom boundary condition, and topographic waves.

Chapter 3 presents the deployment information about the moorings analyzed, along with the numerical model applied in this study, and the necessary information about the setup. In the end, the method used for the EOF analysis is presented.

Chapter 4 presents the different results from both model and observation records.

Chapter 5 contains discussion of the result, including the feature work and conclusion.

Appendix A features additional material of figures and tables.

Appendix B features link to computational codes.

Appendix C features additional material of calculations.

CHAPTER 2

Theory

Following the study by La Lama et al., 2016, the estimated EOFs will be interpreted in terms of baroclinic modes. The modes will not be derived but discussed from theory. This section presents the necessary theoretical framework for this study, starting with the Quasi-Geostrophic Framework. Furthermore, the baroclinic modes derived with 'flat' and 'rough bottom' conditions are presented, and last, topographic waves.

2.1 Quasi-geostrophic framework

Geostrophic motion defines motion where the pressure gradient and the Coriolis parameter are in equilibrium. Quasi-geostrophic (QG), on the other hand, defines motions where the pressure gradient and the Coriolis parameter are close to being in equilibrium. Furthermore, the quasi-geostrophic framework considers only the system's 'slow modes' while ignoring the 'rapid modes'. QG is therefore applied for long time steps when filtering out fast motions, like gravity waves, is preferable (Vallis, 2017).

There are four main assumptions for a quasi-geostrophic system (LaCasce, 2020):

- The Rossby number, $\epsilon = U/Lf$, is small, $\epsilon \ll 1$. U and L are representative characteristic velocity and characteristic length scale, while f is the Coriolis parameter.
- The variations in f over the domain is small, thus for a β-plane, where $f = f_0 + \beta y$, $|\beta L/f_0| = \mathrm{O}(\epsilon)$.
- The bottom topography, h_b, is small compared to the the total depth, h_0, $|h_b|/h_0 = \mathrm{O}(\epsilon)$.
- The surface elevation, η, is small compared to the total depth, $|\eta|/h_0 = \mathrm{O}(\epsilon)$.

The first assumption also states that the relative vorticity, $|\zeta|$ smaller than ϵ, as $|\zeta|$ scales as $\frac{U}{L}$. Under these assumptions are all stated ratios roughly of the same size and equal to the Rossby number. The vertical momentum advection is substantially less than the horizontal advection for synoptical flow. Thus, the momentum equations can be evaluated as $quasi - horizontal$ and approximately 2-dimensional when neglecting the vertical velocity component, w. This section will introduce three different regimes: the baroclinic (BC) mode derived with 'flat' boundary condition, derived with 'rough' boundary condition and topographic mode. A system can exhibit several modes, thus investigating the current's vertical motion in terms of modes can be confusing.

2.2 Baroclinic flow

Baroclinic flow refers to a stratified model, as the density varies with depth. In baroclinic flow, surfaces of constant pressure are inclined to surfaces of constant density, causing the horizontal

pressure gradient to fluctuate with depth. Thus creating a shear in the vertical. The stratified baroclinic QGPV equation with boundary conditions follows:

$$\frac{D_g}{Dt}[\nabla^2\psi + \partial_z(\frac{f_0^2}{N^2}\partial_z\psi)] + \beta\partial_x\psi = -fw_z \tag{2.1}$$

where

$$\frac{D_g}{Dt} = (\partial_t + u_g\partial_x + v_g\partial_y)$$

is the total derivative, and the partial derivative concerning t is denoted ∂_t. Respectively with the other variables partial derivative as well. f_0 is the Coriolis parameter, and β is its derivative with latitude. Both variables are assumed constant and evaluated at the latitude of interest, referred to as β-plane approximation (see appendix C for further information). ψ is the geostrophic stream function reflecting the pressure fields, defined as

$$\psi \equiv \frac{P}{\rho_c f_0} \tag{2.2}$$

where the surface pressure is defined as

$$\Delta P = \rho_c g \Delta\eta,$$

and η is the sea surface height (SSH). Following is the geostrophic velocity, u_g and v_g defined as

$$u_g = -\partial_y\psi, \qquad v_g = \partial_x\psi, \qquad \zeta_g = \bigtriangledown^2\psi \tag{2.3}$$

and ζ_g is the relative vorticity

$$\zeta_g = \partial_x v_g - \partial_y u_g.$$

$N(z)$ is the buoyancy frequency, defined as

$$N^2 = -\frac{g}{\rho_c}\frac{d\rho_0}{dz},$$

where $\rho_0(z)$ is the background density, and ρ_c is a reference density for seawater (roughly 1000 kg/m3). The baroclinic mode may be determined analytically by using particular buoyancy frequency profiles, N, for stratification.

The QGPV equation for baroclinic flow, equation 2.1 concerns the interior, and thus, the boundaries must be treated separately. Accordingly, the rewritten QG-density equation (see appendix) is applied for boundary conditions. There are two mechanisms for vertical velocity to arise from the bottom boundary condition. One mechanism emerges from flow over a sloping bottom, while the other comes from a bottom Ekman layer. The bottom boundary condition is obtained as followed:

$$\frac{f_0}{N^2}\frac{d_g}{dt}\frac{\partial\psi}{\partial z} = -u_g \cdot \nabla h - \frac{\delta}{2}\nabla^2\psi \tag{2.4}$$

The first term on the right-hand side of the equation results from flow over sloping topography, where ∇h is the gradient to the bottom topography. The second term on the right-hand side results from bottom Ekman pumping, where δ is the depth of the layer.

The QG framework considers slow motion and filters out fast motion. Thus, the upper boundary condition is assumed to be 'lid' as the sea surface height can be neglected. Thus, the vertical derivative of the stream function vanishes at the upper boundary:

$$\partial_z \psi|_{z=0} = 0 \tag{2.5}$$

and

$$w_{z=0} = 0$$

.

The rigid lid assumption is a simplification. In reality, the baroclinic mode is accompanied by a sea surface deviation at the maximum gradient in the subsurface density, referred to as the 'thermocline'. The deviation in the sea surface results from horizontal velocities at the surface, causing the interface to deform and creating vertical velocities. As a result, the thermocline is pushed down for downward isopycnal velocities, and the surface rises. The surface rise associated with the Baroclinic mode results in a strong surface signature used to derive BC mode from lateral SSH gradients obtained from satellite observations.

The vertical structure is derived assuming a wave solution in the shape of:

$$\psi = Re\hat{\psi}e^{ikx+ily-iwt} \tag{2.6}$$

where Re refers to the reel part of the wave solution. Equation 2.6 is further substituted into linearized equation 2.1 around time, yielding an ordinary differential equation for the vertical structure, $\psi(z)$

$$\frac{d}{dz}(\frac{f_0^2}{N^2}\frac{d\phi}{dz}) + \lambda^2\phi = 0 \tag{2.7}$$

where

$$\lambda^2 \equiv \frac{\beta k}{w} - (k^2 + l^2), \tag{2.8}$$

λ is the wavelength, and k, l, w is the wavenumber in the x, y, t direction. The equation 2.7 refers to as the "Sturm-Liouville" problem or the eigenvalue problem. Only specific values of λ are accepted for appropriate boundary conditions at the top and bottom. The sign of λ^2 determines the solution of $\phi(z)$; if positive, the solution oscillates; if negative, the solution decays away from the boundary.

This thesis presents two approaches for the bottom boundary condition, resulting in different vertical structures. The first is the classic 'flat bottom' boundary condition, and the second is the 'rough bottom' boundary condition, as recommended by several new studies.

Flat bottom:

The 'flat bottom' approach assumes no topography, thus $h_b = 0$, and

$$\overline{u_g} \cdot \nabla h = 0.$$

To satisfy the kinematic boundary condition, no flow through solid boundary, for $h_b = 0$ must the vertical velocity at the bottom vanish, so $w|_{z=-h} = 0$, so:

$$\frac{\partial \psi}{\partial z}|_{z=-h} = 0 \tag{2.9}$$

Wunsch, 1997 used the 'flat bottom' approach when calculating the baroclinic and barotropic mode. He found the baroclinic signal to have a higher SSH signature than the barotropic mode. At the same time, he noticed that the calculated EOF from current meter records revealed a vertical structure that resembled a combination of the two modes, assuming they canceled each other out at the bottom.

Starting with equation 2.7 and wave solution as equation 2.6, assuming constant stratification, the vertical structure can be obtained

$$\hat{\psi(z)} = A\cos(\frac{N\lambda z}{f_0}) \tag{2.10}$$

For $\psi = 0|_{z\to\infty}$. The baroclinic wave structure, ψ, has various relationships dependent on the mode, n. For n = 0, is $\psi(z)$ constant in the vertical and referred to as the barotropic mode (BT). The BT mode is an independent depth mode, as the horizontal velocities do not change with depth. The BT mode is always present under the condition that the density perturbation disappears on the borders. The first baroclinic mode (BC1) is developed for $n = 1$. BC1 calculated with the 'flat bottom' condition results in the velocity changes sign one time with depth, resulting in a zero-crossing. BC1 with 'flat-bottom' is known to cause the largest variations in the thermocline. The second gravest baroclinic mode is obtained for $n = 2$, crossing zero twice for the 'flat bottom' boundary condition.

Solving for λ:

$$\lambda^2 = \frac{n^2\pi^2 f_0^2}{h^2 N^2} = \frac{n^2}{L_d^2}$$

,

$$L_d = \frac{Nh}{\pi f_0} \tag{2.11}$$

Where $L_d$is the deformation radius for baroclinic Rossby waves. The deformation radius is an essential indicator for when the waves feel the Earth's rotation and is widely used as an indication of the length scale to eddy at different latitudes Lacasce and Groeskamp, 2020. Further solving for the ω obtains the dispersion relation for baroclinic Rossby waves with a flat bottom.

$$\omega = -\frac{\beta k}{\kappa^2 + n^2/L_d^2}, \tag{2.12}$$

where $\kappa^2 = (k^2 + l^2)$.

Rough bottom:

The second approach for the kinematic boundary condition includes topography, $h_b \neq 0$, assuming either 'steep' or 'rough' bottom. The kinematic boundary condition is satisfied for zero horizontal velocity at the bottom, thus

$$\overline{u}(-h) = 0$$

so

$$-\frac{\partial \psi}{\partial y} = 0 \Longrightarrow \psi|_{z=-h} = const. = 0 \tag{2.13}$$

Where ψ is a constant, chosen to be zero. The vertical structure approaches zero with depth for the' rough bottom condition.

Again, solving for equation 2.7 and assume wave solution as equation 2.6, obtains equation for the vertical structure. For the upper boundary condition $z = 0$ and $\frac{\partial \psi}{\partial z} = 0$, and the vertical structure reduces to

$$\hat{\psi}(z) = A\cos\left(\frac{N\lambda z}{f_0}\right)$$

At the lower boundary $z = -h$, the kinematic 'rough bottom' boundary is $\psi = 0$, so the vertical structure becomes

$$\psi = A\cos\left(\frac{N\lambda}{f_0}h\right) = 0$$

thus, either A=0, or $\cos\left(\frac{N\lambda}{f_0}h\right) = 0$, which is true for

$$\frac{N\lambda}{f_0}h = n\pi + \frac{\pi}{2}.$$

Solving for λ

$$L_d^2\lambda^2 = \frac{(n\pi + \frac{\pi}{2})^2}{L_d^2}$$

Thus, the dispersion relation for baroclinic Rossby waves with 'rough bottom' boundary condition becomes

$$w = -\frac{\beta k}{(\frac{(n+1/2)\pi}{L_d})^2 + \kappa^2}. \tag{2.14}$$

For BC1 calculated with the 'rough bottom' condition, the vertical structure approaches zero with depth and does not necessarily exhibit zero crossing.

The baroclinic Rossby wave oscillates over long periods in the Arctic, extending over several years. The period for baroclinic Rossby waves in higher latitudes can be estimated by assuming a deformation radius of about $Ld = 10$ km, a good approximation for the Arctic. However, for long

waves, the wavenumber, *kappa*, becomes substantially smaller than the other terms in the equation 2.14, thus may be neglected.

The period, $T = \frac{2\pi}{w}$, of a 'rough bottom' BC Rossby wave at 70° degree north can be calculated using $\beta_{70^\circ} = 7,8 * 10^{-12}$. Assuming $k \sim \frac{1}{L_d}$ the dispersion relation for baroclinic Rossby waves with a 'rough bottom' boundary condition is reduced to $w \sim \beta L_d$, and the period becomes

$$T_{70^\circ} = \frac{2\pi}{\beta L_d} \simeq 2.55 yr^{-1}$$

.

2.3 Topographic waves

Topographic waves are Rossby waves supported by the bottom topography instead of the β-effect. Starting with the QGPV equation on the f-plane, so $\beta = 0$

$$\frac{D_g}{Dt}[\bigtriangledown^2\psi + \partial_z(\frac{f_0^2}{N^2}\partial_z\psi)] = 0 \tag{2.15}$$

The fluid's PV is assumed to be constant with time and can be set to zero in the interior. Assuming linear topographic slope, we set the boundary condition to be

$$h = h_0 - \alpha y$$

so $h_b = \alpha y$. Solving the bottom condition equation for linear slope and assuming wave solution 2.6 and constant stratification, the vertical structure is obtained, decaying upward from the bottom boundary

$$\hat{\phi}(z) = Ae^{-NKz/|f_0|} \tag{2.16}$$

The wave has a vertical e-folding scale of : $H \propto \frac{|f_0|}{NK} = \frac{|f_0|\lambda}{2\pi N}$, thus the vertical extend dependent on the horizontal scale. Topographic waves arise from the conservation of potential vorticity when the water column stretches/squashes in response to changes in the topography and are frequently observed over continental slopes. For the 'rough bottom' BC mode are bottom intensified topographic waves accounting for velocity fluctuations at the bottom, replacing the BT mode altered by the bathymetry LaCasce, 2017.

CHAPTER 3

Observations, model and methods

This chapter introduces the observation records obtained from the moorings deployed around the Arctic and sub-Arctic region, along with the essential information about the numerical ocean model applied in this study. All mooring stations have a corresponding research report with additional details about the data, which can be found in the end of this section. In addition, more detailed information regarding the model setup is described in 'A high-resolution ocean and sea-ice modeling system for the Arctic and North Atlantic oceans' article Dupont et al., 2015, and in the ocean engine of NEMO, manual Gurvan et al., 2017.

The section will present the mooring records first, as observation data are crucial for an exact representation of the Arctic ocean. Further, introducing the numerical model before ending this chapter explains the method applied to conduct the EOF analysis.

3.1 Current meter records

Acoustic Doppler Current Profiler (ADCP) records from moorings deployed in the Arctic and sub-Arctic region provide in-situ observations to characterize the Arctics ocean's vertical structure. The observation records are further employed to verify the model performance. This study analyzes 19 moorings obtained from a variety of sources. An overview of the station depth, location, and deployment for each mooring is presented in Table 3.1. The current meter data contains time and depth records of u- and v-velocities (North-ward and East-ward, respectively). The velocity records are further rotated along and across the principal direction of horizontal variability, EOF1, and EOF2, obtained from horizontal EOF analysis. Finally, the vertical structures are estimated by vertical EOF analysis on the rotated velocity data. The research projects from the Lofoten region, Yermak Plateau, and North of Svalbard conducted the mooring records over a single year. The Lofoten moorings are deployed between 2016 and 2017, with an along-isobath distance of 26km between North-South moorings (MN and MS) and a cross-isobath distance between North to West (MN and MW) of 6 km Fer, 2020.

Six moorings were deployed North of Svalbard, to the East and West on the continental slope. The West located moorings have a cross-isobath distance between W1 and W3 of 34 km, and the East located moorings have a cross-isobath distance of 18 km. The along isobath distance between the West and East moorings is 94 km. The moorings deployed at Yermak Plateau between 2014 and 2015 have two deeper stations on the slope, Y1, and Y3, and one shallower on the Plateau, Y2. The data from Yermak Plateau are hourly averaged and vertically gridded at 5dbar seawater pressure levels Fer and Peterson, 2019. All Lofoten and Yermark Plateau moorings were equipped with RDI ADCPs, recording ocean currents in Earth coordinates. The RDI ADCP used is either a 75KHz instrument profiler, averaging every 1 hour, or a 300KHz instrument profiler, ensemble every 1 hour. The two shallow west located moorings north of Svalbard, W1, and W2, in addition to the east mooring, E2, was equipped with an ADCP RDI 75 kHz hourly averaged ensembles, while the downward-looking (upward looking on E1, RID 300 kHz) ADCP RDI 150 kHz at W2, E2

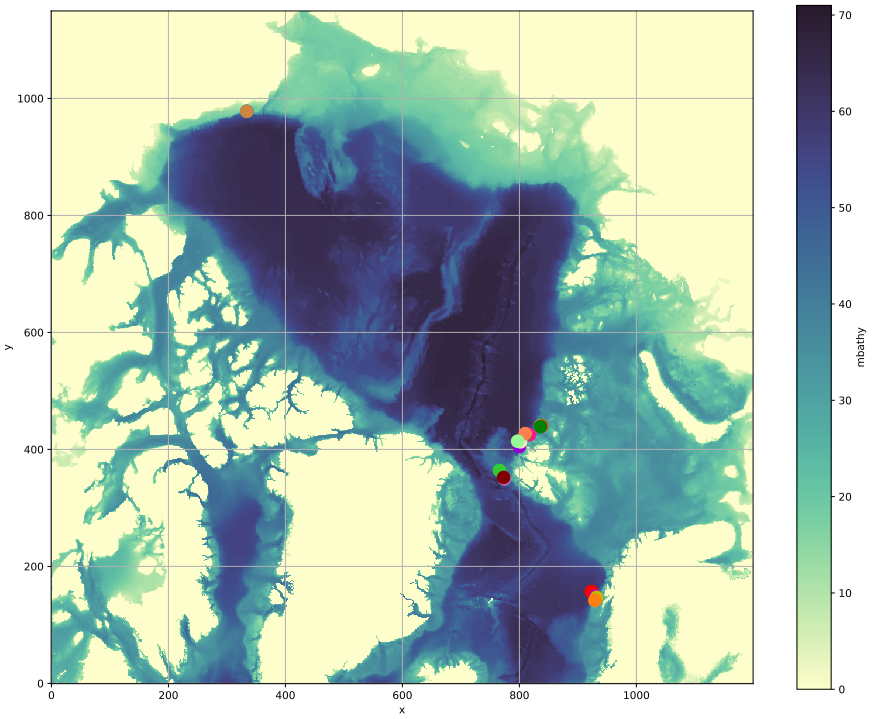

Figure 3.1: Map over the Arctic and sub-Arctic region. The colorbar to the right indicating the different model levels, where zero is at the surface and 75 is at the deepest point of the Arctic ocean. The color dots indicate the location to the deployed moorings analyzed in this study.

and E1 recorded 20-minute averages. The distance between each measurement point on the ADCP varies from 4 meters to 8 meters, depending on the instrument.

The Beaufort shelf and the Barents Sea moorings are conducted over three years at approximately the exact location. The Beaufort shelf moorings executed between 2011 and 2018 are measured with a 300KHz ADCP and a 75KHz ADCP, and the Barents Sea moorings executed between 2013-and 2019 are measured with a RDI 153.6 kHz broadband ADCP. The 2013 mooring has a bin height of 4 meters, while the 2015 and 2017 moorings have 8 meters.

Links to the moorings:

- Barent Sea: Sundfjord, 2021,
- Lofoten: Fer, 2020
- Yermark Plateau: Fer and Peterson, 2019
- Beaufor Seat: Robert, 2020
- North of Svalbard: Ilker, 2022

3.2 The numerical ocean model; CREG12.L75

CREG12.L75 (Canadian REGional) configuration is developed as a part of the CONCEPTS (Canadian Operational Network of Coupled Environmental PredicTion Systems) initiative in collaboration with Mercator Ocean in France and is a high-resolution ice-ocean model covering the North Atlantic and the Arctic ocean. The model is developed to provide Canada with short-term ice-ocean predictions at high resolution. The model output has a time resolution of 5-days, where 73 measurements (spanning a year) is used in this study.

Model Domain

The numerical ocean model simulation, CREG12, used the global ORCA12 domain, with a nominal horizontal resolution of 1/12° in longitude and latitude. The domain reaches from 27°N and includes the whole Arctic. The geographical coordinates system often applied in ocean modeling are three-dimensional orthogonal grids on the sphere, with the North Pole as a singular point. Singular points are not easily treated in a global model without filtering and thus are not optimal for a high latitude numerical ocean model. The solution applied by the ORCA grid is a tripolar grid system that allows for constructing a global orthogonal curvilinear ocean mesh (i.e. the position of all the scalar and vector points) with two north mesh poles placed on the land. Thus, the ORCA mesh grid has no singular point inside the ocean domain, leading to a loss of continuity as the grid system is not composite. The ocean mesh is defined by transforming from a geographical coordinate system (λ, ψ, z) into a curvilinear coordinate system (i,j,k). It uses a generalization to three dimensions C-grid in Arakawa's classification, widely used in ocean modeling due to it being favorable for conservation properties (Dupont et al., 2015). The C-grid has various variables situated at different locations. The scalars are placed in the grid cell center, with the vector components along the faces. The u-velocity is in the East-West direction, and the v-velocity is in the North-South orientation of the cell face. The horizontal grid consists of 1580x1801 grid points but is reduced to 1150x1200 topics for this thesis, covering the Arctic Ocean from 58° N to 90°N. The horizontal resolution varies, with an average of 5km in the Arctic and a Rossby deformation radius of 10km. The model is eddy-resolving in the central Arctic ocean.

The vertical resolution of the model is divided into 75 z-levels, with the bottom level at 5902 meters into the Arctic Basin. The distance between the levels varies and is not evenly distributed. The bathymetry used is taken from the ORCA12-T321 run of Mercator Océan. The model uses partial bottom steps for accuracy to receive a realistic representation of the irregular bathymetry. The bathymetry has a minimum depth of 20 meters.

Boundary conditions

The model has two vertical and one complex horizontal boundary along the coastlines. The lower boundary is at surface $z = -H(i, j)$, where H is the total water column height measured from the surface down to the sea bed. The upper boundary, either an air-sea or an ice-sea interface, is defined by the surface elevation, η, at surface $z = \eta(i, j, k, t)$. Both boundaries are related to a reference surface at $z = 0$, taken as the mean sea surface. Between these surfaces, the ocean exchange different fluxes, such as heat, freshwater, salt, and momentum, with the earth's crust and continental margins, sea ice, and the atmosphere, deciding the ocean's conditions.

The surface boundary condition is dependent on the surface stress, τ_{wind} & τ_{ice} imposed by wind and the sea ice, heat fluxes from incoming solar and non-solar heat fluxes (Q_{ns}, Q_{sr}), and the virtual salinity flux associated with the freezing and melting of seawater. In addition to the surface stress, the atmospheric pressure, tidal potential, and snow and ice mass can contribute to the surface pressure gradient. Thus are also included in the dynamical forcing equation. The essential land-ocean exchange is through freshwater input from river runoffs. Freshwater alters the density of seawater, particularly near the surface interface, resulting in less dense water. Therefore, the model includes river runoff for long-term integration, where the runoff can affect the properties of

the water masses formation. Ice shelf and sea-ice melting and refreezing are additionally included in the freshwater budget.

The freshwater budget is particularly important at high latitudes, as salinity fluctuations dominate the density gradient. The kinematic surface condition, which includes the fresh water input (PE) and evaporation (E), can be expressed as

$$w = \frac{\partial \eta}{\partial t} + U_{h|z=\eta} \cdot \bigtriangledown_h(\eta) + PE - E. \tag{3.1}$$

The freshwater budget includes both exchange with the atmosphere and possibly with the sea-ice and ice shelve. The dynamic surface boundary condition is computed as a continual pressure over the interface $z = \eta$ in combination with horizontal momentum from wind and sea-ice stress acting on the surface and heat exchange between the atmosphere-ocean/ice-ocean.

Except for momentum, most of the exchange between the solid ground and the ocean ignores on all scales. The bottom friction momentum is parameterized using bottom and/or lateral boundary conditions for turbulent flow. The bottom flow is parallel to the bathymetry to satisfy the no flow through solid boundary conditions. Thus, the kinematic boundary condition becomes

$$w = -U_h \cdot \bigtriangledown_h(H). \tag{3.2}$$

The sea ice-ocean fluxes consist of heat, salt, freshwater, and momentum. The ice-ocean interface is constrained to surface temperature at a freezing level in the model. The surface boundary condition includes the freezing and melting cycle associated with fresh water and salt fluxes.

Initial conditions and forcing

The model has two sets of initial ocean conditions. A reanalysis with high compliance with observation at a lower latitude but less accuracy at higher, named GLORYS2v1. The second initial condition is obtained from the ORCA12-T321 run of Mercator Ocean, with enhanced performance in the Arctic Ocean. The ice cover is abstracted from the same set of initial conditions, whereas the river freshwater discharge is from the monthly climatology of Dai and Trenberth.

The model starts the ocean at rest to be initialized by two active tracers, the potential temperature, and salinity fields. An active tracer influence the current directly by altering properties in the equation of motion. Temperature and salinity are active tracers as they determine the water's density. The prognostic field equations can be summarized as follows:

NXT = ADV + LDF + ZDF + SBC (+QSR) (+BBC) (+BBL) (+DMP)

Where the four latter are optional, NXT refers to time-stepping, ADV to advection, LDF to lateral diffusion, and ZDF to the vertical diffusion. The last five terms in the equation are external forcing terms, with the four lateral optional. NSBC stands for Surface Boundary Condition, QSR for penetrative Solar Radiation, BBC for Bottom Boundary Condition, BBL is the parameterized contribution from the bottom boundary layer, and DMP is the internal damping. The model has three additional dynamical forcing parameters to the surface and bottom stressed, imposed as boundary conditions. The atmospheric pressure, tidal potential, and snow and ice mass are all included when calculating the surface pressure gradient.

3.3 Principal Component Analysis/Empirical Orthogonal Functions

Empirical Orthogonal Functions (EOF) are a type of the statistics analyzing method, principal component analysis (PCA), frequently employed in climate studies to investigate possible spatial

modes of variability and how they evolve *Analysis tools and methods* n.d. The goal is to minimize the dimensions of large data sets while retaining the majority of the data set's variance. The EOFs are new uncorrelated variables created by combining existing ones, with the first EOF carrying the most knowledge and the last EOF containing the least. The EOFs are derived by solving the eigenvalue problem of the covariance matrix, A, produced from velocity data at a specific point is solved. The eigenvalue problem determines the eigenvalues, λ, and related eigenvectors, x.

$$Ax = \lambda x, \tag{3.3}$$

The eigenvalue problem relates the covariance matrix to a linear transformation. The eigenvectors are unit vectors in the direction of the largest variance to the data set and are unchanged after the linear transformation. The eigenvalue is the corresponding magnitude of the variance to the eigenvector. Thus, the eigenvalues and eigenvectors measure the percent of explained variance (PEV) by the mode and shape of each mode, respectively.

$$PEV = \frac{\lambda_i}{\Sigma_{i=1}^{n}\lambda} \tag{3.4}$$

The EOFs are used to project the original data onto, creating a new coordinate system in the direction of the most considerable variability.

The covariance matrix, $A_{i,j} = \sigma(x, y)$ where, $\sigma(x, y)$ is the covariance between the variables x and y, $A \in R^{d\times d}$ and d describes the number of dimension or variables of the data set. The covariance is a symmetric matrix, with the variance in the diagonal and the covariance of the variables else. The variance and the covariance are defined as

$$\sigma_x^2 = \frac{\Sigma(x_i - \mu)^2}{n-1}, \tag{3.5}$$

$$S_{x,y} = \frac{\Sigma(x_i - x)(y_i - y)}{(n-1)}, \tag{3.6}$$

Where σ^2 is the variance and $S_{x,y}$ is the covariance. The variance is a non-negative number indicating the spread of the values to the variable, thus indicating how closely the distribution is around the expected value. A more significant variance implies more scattered observations. The covariance is a measure of how the variables change together. For a positive number, the variables correlate, thus increasing decrease together, but for a negative number, they are anti-correlated.

Table 3.1: Details of Mooring Deployments

Location:	Mooring	Deployment	Latitude/Longitude	Echo depth
A-TWAIN, Barent Sea continental slope	d13	22.09.2013-15.09.2015	81°24.202'N 31°13.247'E	133m
A-TWAIN, Barent Sea continental slope	d15	19.09.2015-17.09.2017	81°24.255'N 31°13.533'E	133m
A-TWAIN, Barent Sea continental slope	d17	22.09.2017-18.11.2019	81°24.587'N 31°14.506'E	178m
Lofoten, Basin	MB	02.06.2016-09.09.2017	69°52.89'N 011°11.89'E	2925m
Lofoten, South	MS	31.05.2016-08.09.2017	68°50.128'N 012°44.77'E	670m
Lofoten, North	MN	01.06.2016-08.09.2017	68°56.06'N 013°20.24'E	645m
Lofoten, West	MW	01.06.2016-08.09.2017	68°58.759'N 013°16.845'E	1500m
Yermark, North of Fram Strait	y1	10.09.2014-13.08.2015	79°37.209'N 05°57.541'E	1535m
Yermark, North of Fram Strait	y2	10.09.2014-13.08.2015	80°03.876'N 05°48.733'E	850m
Yermark, North of Fram Strait	y3	11.09.2014-13.08.2015	79°44.093'N 05°56.333'E	1209m
Beaufort Shelf	ANO12	16.10.2012-16.10.2013	71°23.64'N 152°2.91'E	147m
Beaufort Shelf	ANO14	18.10.2013-17.07.2014	71°23.64'N 152°2.91'E	147m
Beafort Shelf	ANO16	19.07.2014-07.09.2016	71°23.659'N 152°3.04'E	147m
Beaufort Shelf	ANO18	08.09.2017-30.10.2018	71°23.66'N 152°3.5'E	147m
North of Svalbard	E1	16.09.2018-23.09.2019	81°24.925'N 24°00.000'E	300m
North of Svalbard	W1	15.09.2018-21.09.2019	81°10.979'N 18°29.052'E	401m
North of Svalbard	E2	16.09.2018-23.11.2019	18°30.813'N 23°59.853'E	706m
North of Svalbard	W2	25.09.2018-21.09.2019	81°22.686'N 18°23.789'E	727m
North of Svalbard	E3	16.09.2018-23.11.2019	81°35.453'N 23°59.982'E	1222m
North of Svalbard	W3	20.09.2018-21.11.2019	81°27.356'N 18°23.730'E	1202m

CHAPTER 4

Results

This chapter presents on the results from the numerical ocean model and the observation records obtained from moorings stationed around the Arctic and sub-Arctic. First, the velocity statistics from the model data is considered, providing an overview of the general circulation in the Arctic. Thereafter, the estimated vertical EOFs from both model and observation data are evaluated. To conveniently compare the two methods, the model EOFs are derived from equivalent locations to the moorings, hereafter referred to as stations. Additionally, the observation records are averaged over a five-day estimate to obtain the same temporal resolution as the model EOFs. However, since the five-day estimate demonstrated an almost identical structure as the original observation EOFs are they not visualized.

To find the principal direction of flow variability, the two primary EOFs derived from the horizontal current are used to rotate the velocity records at each station. The velocity records are rotated after the principal flow direction to identify the impact of topographic steering. The horizontal EOF1 is parallel to the largest fraction of horizontal variance, whereas the second EOF2 is in the direction of the largest fraction orthogonal to EOF1. Therefore, if the topography guides the flow, an anisotropic relationship is expected between horizontal EOF1 and EOF2, as a significant fraction of the variance is anticipated to be parallel to the topography.

The observation records contain measurements errors and lack data for specific points. Most of these errors occur near the top and bottom of the moorings vertical range, but they may however, also occur in the middle range. These data points without information are referred to as none existing values or nan-values. Because the computational construction of the EOFs can not handle nan-values in the data set, the nan-values were substituted with zero. As zero is a value, it affects the EOF, and can result in misguided results. The optimal choice would be to remove the nan-values from the data set. However, then whole rows or columns would have to be excluded from the data set, as each time-step needs to have the same number of measurement points. Consequently, this would reduce the data set substantially. As the master thesis is confined to a year, the zero substitution was the preferable choice with the time and resources available. In response to the problem of potentially misguided results, especially close to the first and last measurement, the total variance estimated with depth is derived from each observation record. The total variance is derived by removing the nan-values and consequently does not contain substituted zeros. Comparing the EOF to the total variance indicate whether the EOFs demonstrate a correct measured decreasing/increasing. For the total variance and EOFs agreeing, the EOFs are believed to be reliable. However, when not agreeing, the EOFs are considered to be misguiding.

Eventually, EOFs are derived from the numerical ocean configuration, CREG12, solemnly. The high-resolution ocean model functions as a model reality, expanding the measurement locations in order to obtain data from everywhere in the Arctic Ocean. By applying a numerical ocean model, a broader selection of data locations are obtained, thus, the desired dynamic properties can be selected. The new model EOFs are derived from regions experiencing sea ice cover and regions free from sea ice over steep and flat bottom topography to distinguish what characterizes different features in the Arctic.

4.1 An overview of the flow field and its variability.

Velocity statistics derived from the numerical ocean model have been calculated and examined. Velocity statistics is considered as flow has a short length and time scale, thus inherently poor predictability. Horizontal time-averaged velocity and variation ellipses are derived from different depths and analyzed. Investigations of the horizontal flow regime for currents in the Arctic at different depths reveal a general overview of how the vertical structure is depicted. The aim is to distinguish how the flow regime varies with depth, to better understand the vertical structure of the Arctic ocean. The figures in this section are subsampled for every 20 data points and are not smoothed.

Time averaged currents

Time-averaged velocity derived from 35 meters, from 333 meters and from the bottom, are visualized in Fig.4.1, Fig.4.2 and Fig.4.3. The arrows indicate the velocity direction, while the color denotes the strength and is visualized in the colorbar below the figures. The dominant features in the surface velocity, Fig.4.1, are the flow through the openings to the Arctic. Both the Bering Strait and South of the Fram Strait demonstrate velocities larger than five cm/s. In the Norwegian Sea, cyclone flow around the Norwegian Basin and anticyclone flow around the Lofoten Basin are illustrated. The regions experience strong air-sea cooling, characterized by weak planetary velocity and stratification, which are dominant features causing topographic steering. Thus, the mean flow is expected to be predominantly along the bottom topography (Trodahl and Isachsen, 2018). For regions where the isobaths are closing themself, such as around the Norwegian and Lofoten Gyres, cyclone or anticyclone flows are anticipated, depending on the bottom topography and location. Also the the Barents Sea demonstrate more substantial velocities, with less distinct direction. The Barents Sea is shallow, with an average depth of $\sim$200 meters. Thus, the boundaries affect a greater fraction of the water column. The velocity becomes less intensive and largely homogeneous in the Arctic Ocean basin, both in strength and direction. An anticyclone flow pattern over the Canadian Basin with the transpolar drift crossing Lomonosov Ridge around 90 degrees North, is illustrated. The Eurasian Basin illustrate flow direction towards the Fram Strait. Along the continental slope is a cyclone compensation current visible. The model demonstrates a flow pattern consistent with observations. A high pressure is present over the Beaufort sea (referred to as Beaufort high), causing anticyclone flow in the Canadian basin and a cyclon current, transporting Atlantic water around the boundary of the Eurasian Basin. As the model and observations agree, the wind is the dominant dirver for the ocean currents in the model Timmermans and Marshall, 2020.

The subsurface model current derived from 333 meters depth is visualized in Figure 4.2. Consistent with expectations, the velocity has decreased from the surface over the whole domain. Again, the dominant features are the Norwegian coastal current and the West Spitsbergen Current, and the East Greenland Current. The velocity is more substantial near the boundaries, decreasing further into the basin for the subsurface current. In contrast, the surface current appeared more homogeneous in strength over the whole domain. In addition, the direction in the pool region is more irregular, suggesting variations in the bottom topography has a greater signature deeper in the water column. The topographic steering is more profound along the continental slopes, and the arrows parallel the isobaths over steep terrain for the entire region. The flow predominantly follows the ridge over Lomonosov ridge and Gakkel ridge, unlike the surface current, which crosses over towards Fram Strait.

Figure 4.3 shows the bottom velocity for the Arctic and sub-Arctic region. Bering Strait and the Barents Sea revile the most significant bottom velocity. Both regions are substantially shallow, as the average depth in the Bering Strait is 50 meters and in the Barents Sea 200 meters. The averaged bottom velocity in the Bering Strait is greater than $>$4 cm/s and $\approx$4 cm/s in the Barents sea. In deeper pool regions, the bottom velocity is close to zero. The flow direction is more inconsistent at the bottom than higher in the water column. The flow direction is predominantly downward on the Norwegian continental slope, indicating cross isobath flow. Thus, vertical velocities are expected,

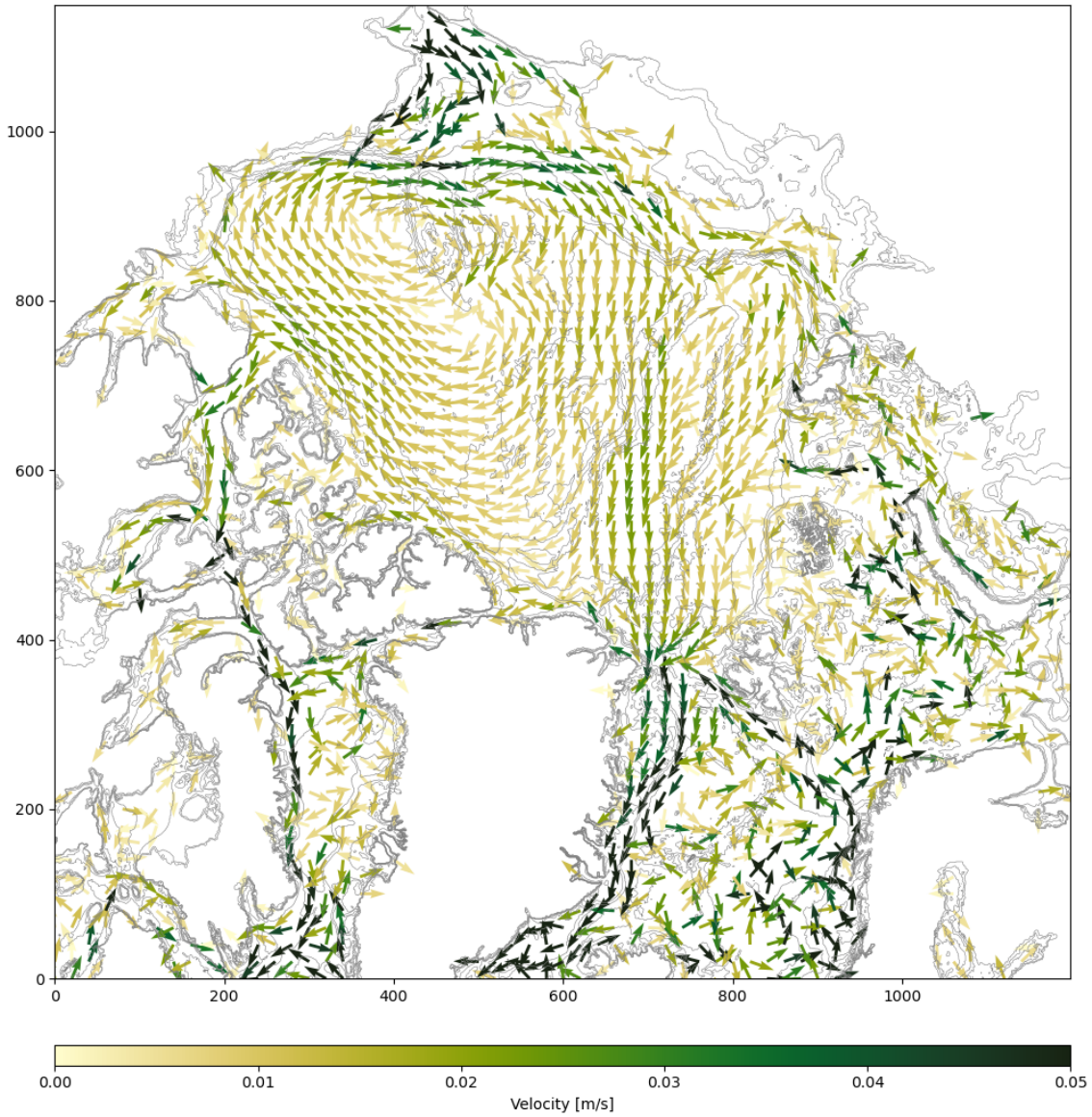

Figure 4.1: Time averaged velocity at 35 meters depth in Arctic and sub-Arctic region. The direction of the arrows indicate the current direction, while the color of the arrow indicate the strength and can be read of from the colorbar at the bottom.

and one may assume topographic waves to emerge (Trodahl and Isachsen, 2018). The Beaufort Sea also reveals cross isobath flow direction, as the arrows seem to be towards the coastline of Canada. The velocity in the Barents sea is more consistent with the topography again, as most arrows are aligned with the isobaths. The model has a high-resolution bathymetry grid with an average of 5km. Thus, irregularity in the current direction may result from the topography at the measuring point not demonstrating the averaged slope direction, as the bathymetry may curvature and bend along the isobaths.Also, the subsampling may lead to bias, as the data point visualized may not represent the general direction.

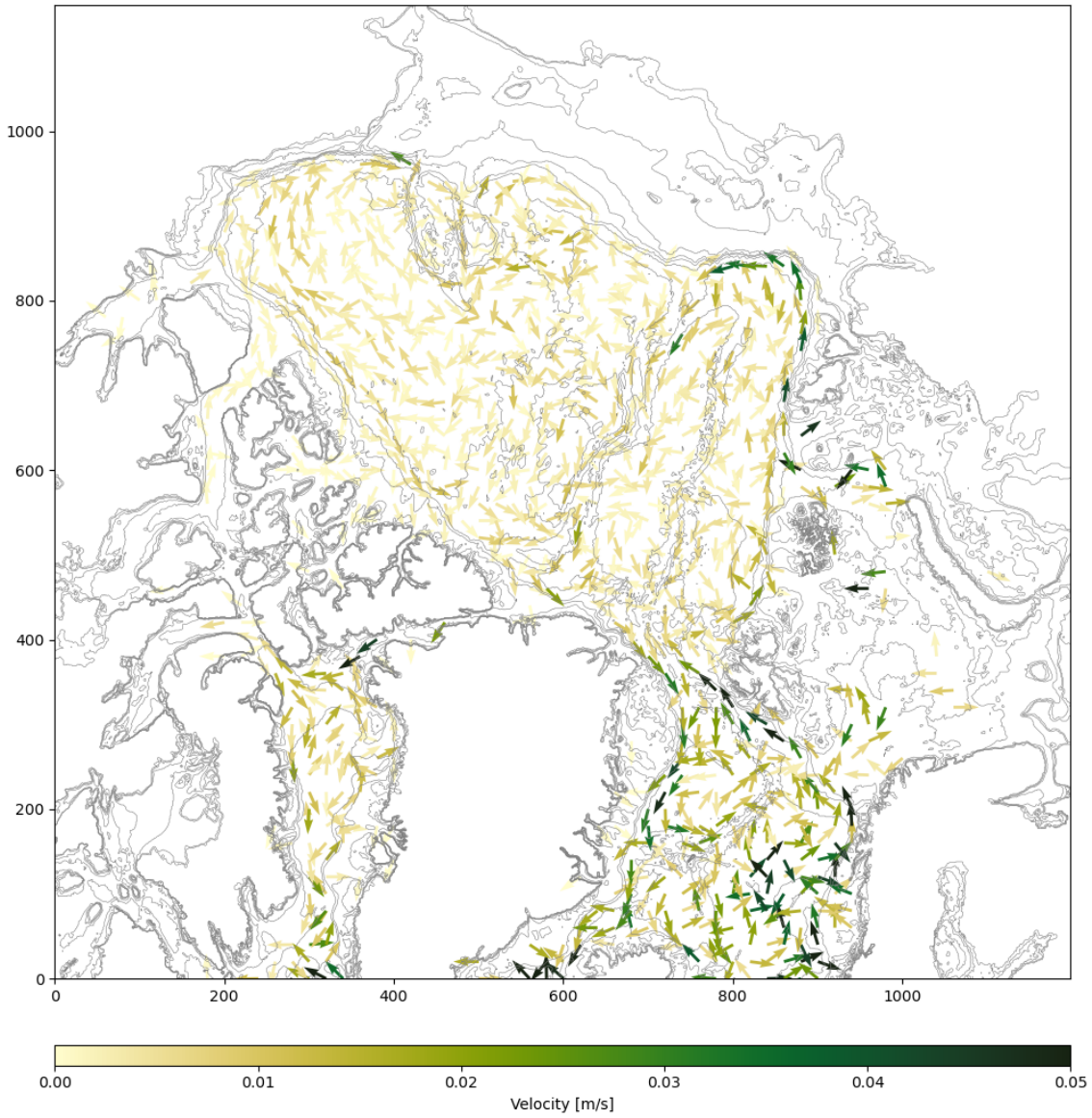

h

Figure 4.2: Time averaged velocity at 333 meters depth in Arctic and sub-Arctic region. The direction of the arrows indicate the current direction, while the color of the arrow indicate the strength and can be read of from the colorbar at the bottom.

Horizontal variance ellipses

Variation ellipses are calculated and visualized for the same depths as the time-averaged velocity to see how topography impacts the direction of flow variability. The variation ellipses are derived using principal component analysis. The ellipse's main axis corresponds to the dominant EOF (EOF1), indicating the principal direction of variability as it capturing the greatest fraction of the current fluctuations. The minor axis corresponds to the second EOF (EOF2), capturing the most considerable fraction of the velocity variations orthogonal to EOF1.

Fig.4.4 illustrates variance ellipses derived from 35 meters depth. The greatest variance is visualized for the same regions as for the averaged velocity, Fig.4.1. The ellipse's orientation is challenging to

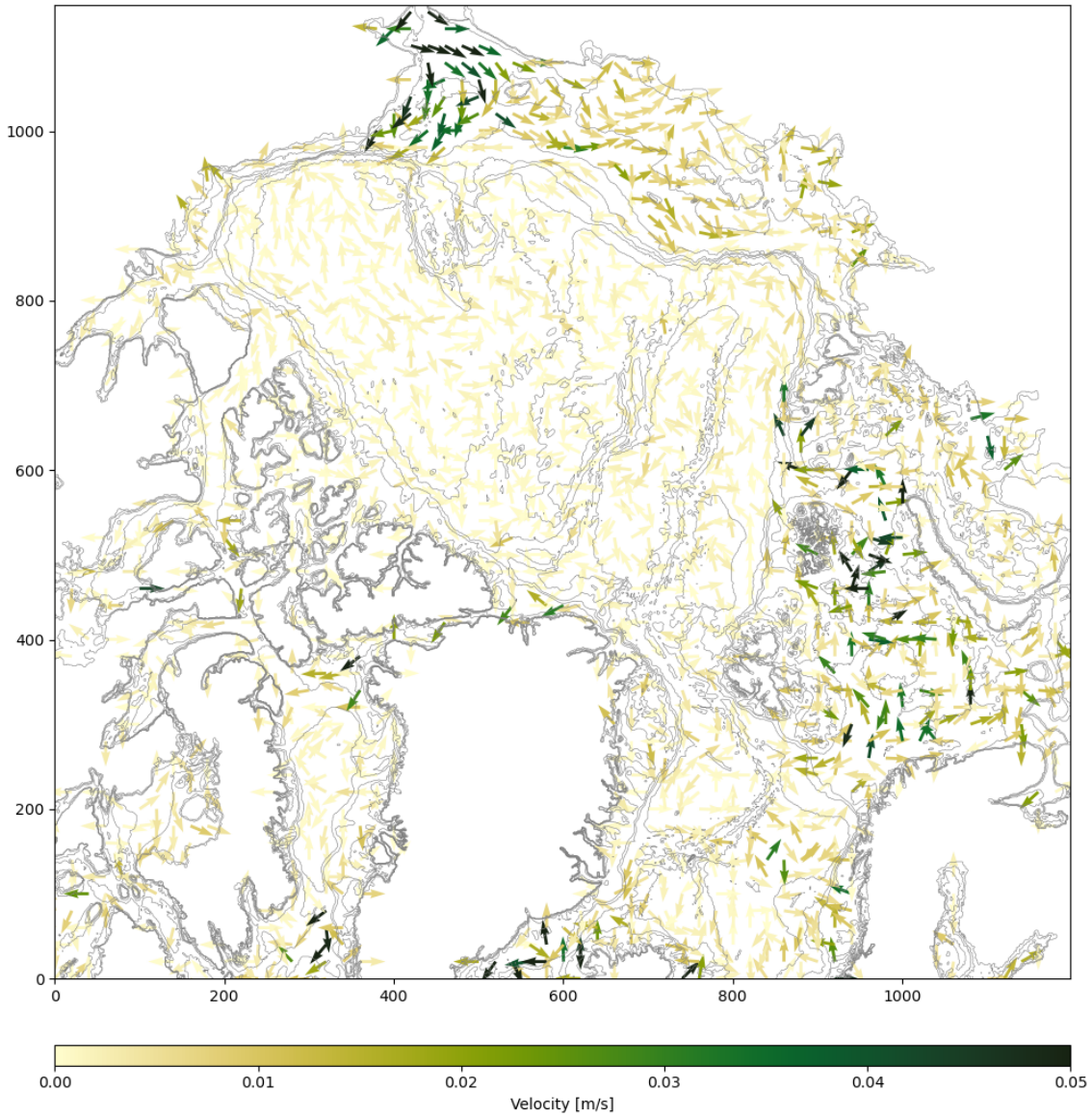

Figure 4.3: Time averaged velocity for the bottom current in Arctic and sub-Arctic region. The direction of the arrows indicate the current direction, while the color of the arrow indicate the strength and can be read of from the colorbar at the bottom.

establish, as the velocity is substantially higher at along the Norwegian coast than in most of the Arctic ocean. Therefore, an additional figure zoomed in on the Norwegian coast is included from 35 meters depth, Fig.4.5, so the orientation is easily read. A clear favorable direction along the coast of Norway and Greenland is visualized. Thus indicating topographic steering. The variance increases away from the shelf and onto the slope. The variance is noticeably larger in shallower regions, compliance with the averaged velocity, indicating stronger velocity in shallow regions, and areas experiencing strong currents. The Barents Sea mainly demonstrate anisotropic variance ellipses, following the opening on the East side and along the continental slope, indicating strong regional topographic control. Topographic steering is visualized along the boundaries, as the continental slope. Moving away from the slope and onto deeper water, the variance decreases and the ellipses become more isotropic. The weak basin current makes the orientation hard to establish as the

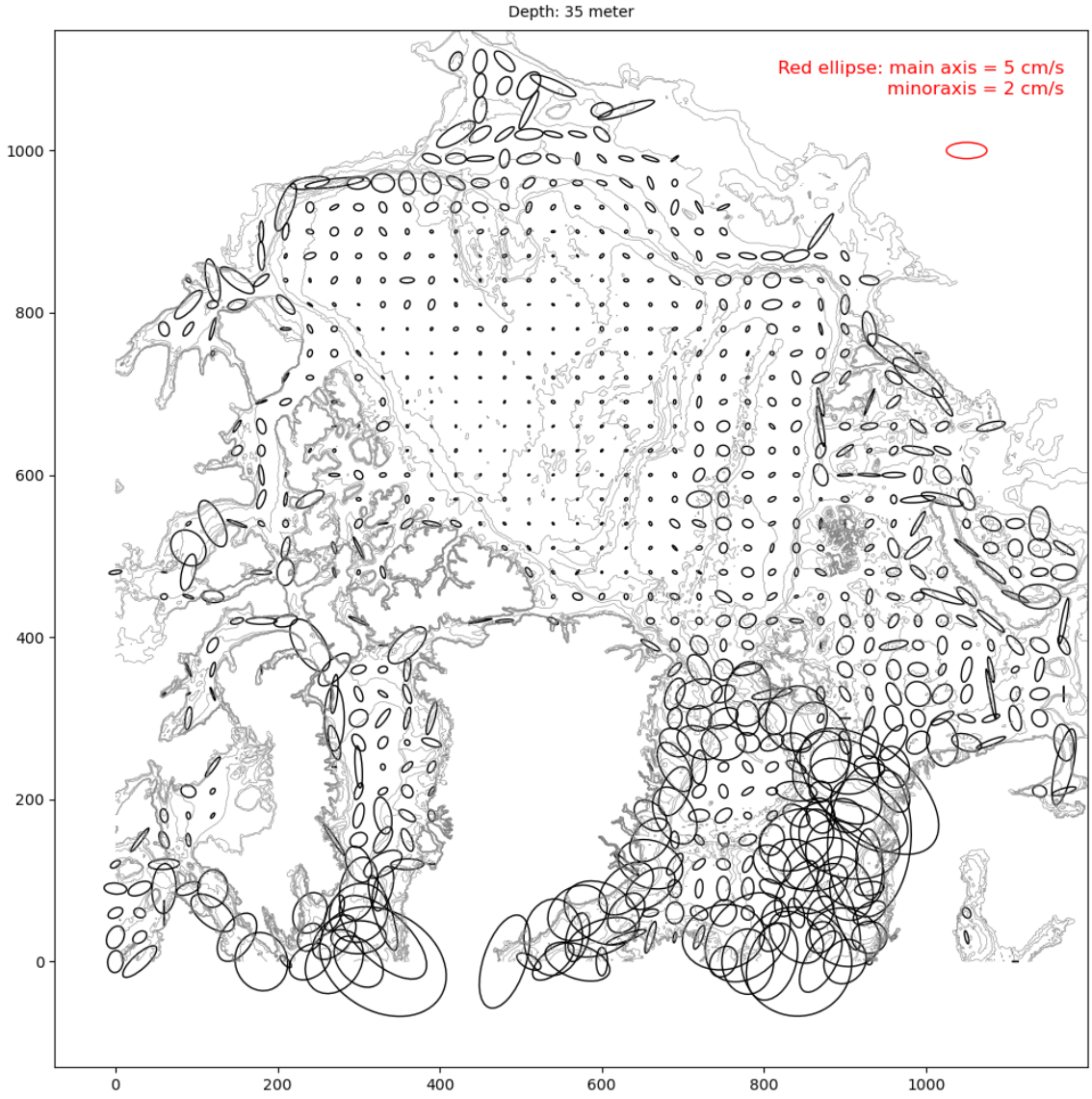

Figure 4.4: Horizontal variance ellipses for the current at 35 meters depth, in Arctic and sub-Arctic region. The main axis of the variance ellipse capture the majority of current direction, while minor axis capture the second largest portion of the current, orthogonal to the main axis. The size of the ellipses indicates the current strength. The variance ellipse marked in red is demonstrating the average current velocity, relative to the other ellipses. The strength of the red ellipse can be read in red to the upper right side.

variance ellipses are small but suggest a more irregular orientation. The variance increases over the Gakkel Ridge, separating the Amundsen and Nansen basins, but remains predominantly isotropic.

Figure 4.6 illustrate variance ellipses derived from 333 meters depth. The variance decreases significantly over the whole domain. Greater variance is again found in the same location as for shallower depth. The topographic steering is more profound along the continental slope around the Barents sea opening and Siberia, as the ellipses have become more anisotropic. The currents are weaker in Chukchi, Beaufort, and along the coast of Canada. Thus, it is harder to establish the

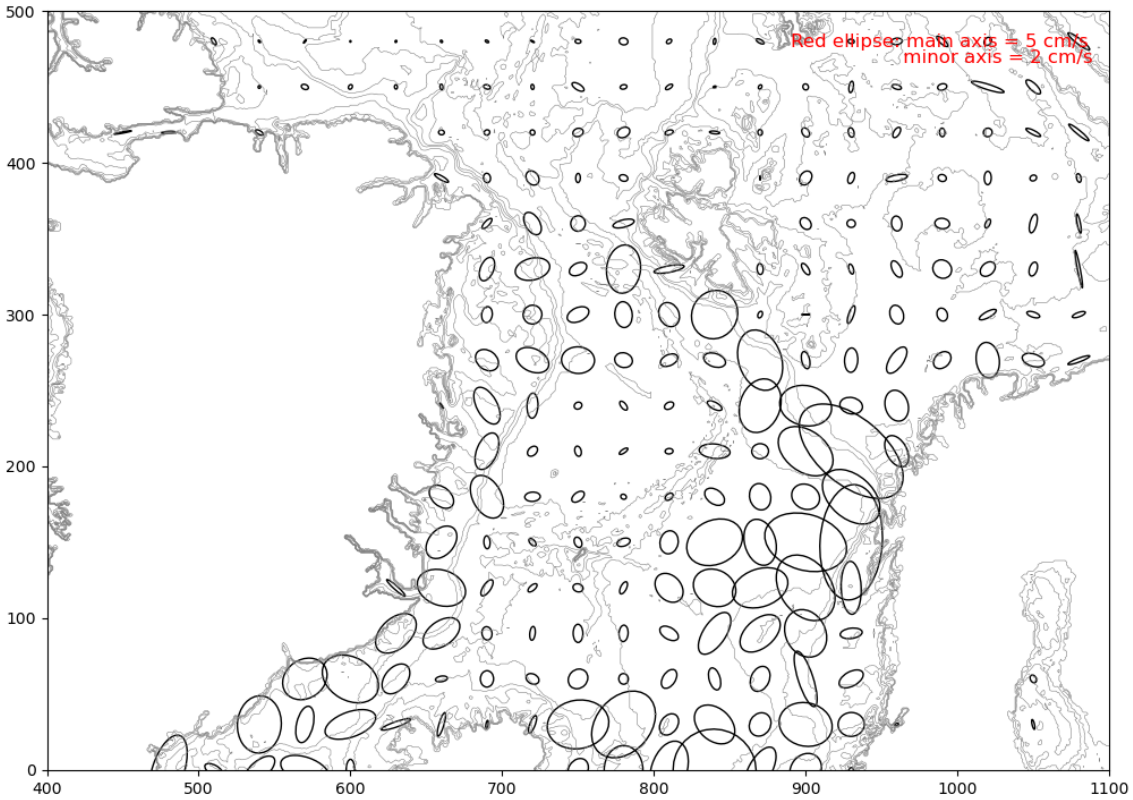

Figure 4.5: Horizontal variance ellipses for the current at 35 meters depth, zoomed in on the Norwegian coast. The main axis of the variance ellipse capture the majority of current direction, while minor axis capture the second largest portion of the current, orthogonal to the main axis. The size of the ellipses indicates the current strength. The variance ellipse marked in red is demonstrating the average current velocity, relative to the other ellipses. The strength of the red ellipse can be read in red to the upper right side.

flow fluctuation.

Figure 4.8 illustrates variation ellipses derived from the bottom current. Shallower regions reveal more considerable variance, consistent with the time-average velocity shown in Fig.4.3. The variance is predominantly anisotropic along the bottom. However, the orientation is not always parallel to the topography, as one might assume. Instead, the variance ellipses cross the isobaths multiple times at different locations. Again, as mention for the averaged velocity, may this result from noise or the subsampling. Some ellipses visualized in Fig.4.8 emerge as a line and may result from the

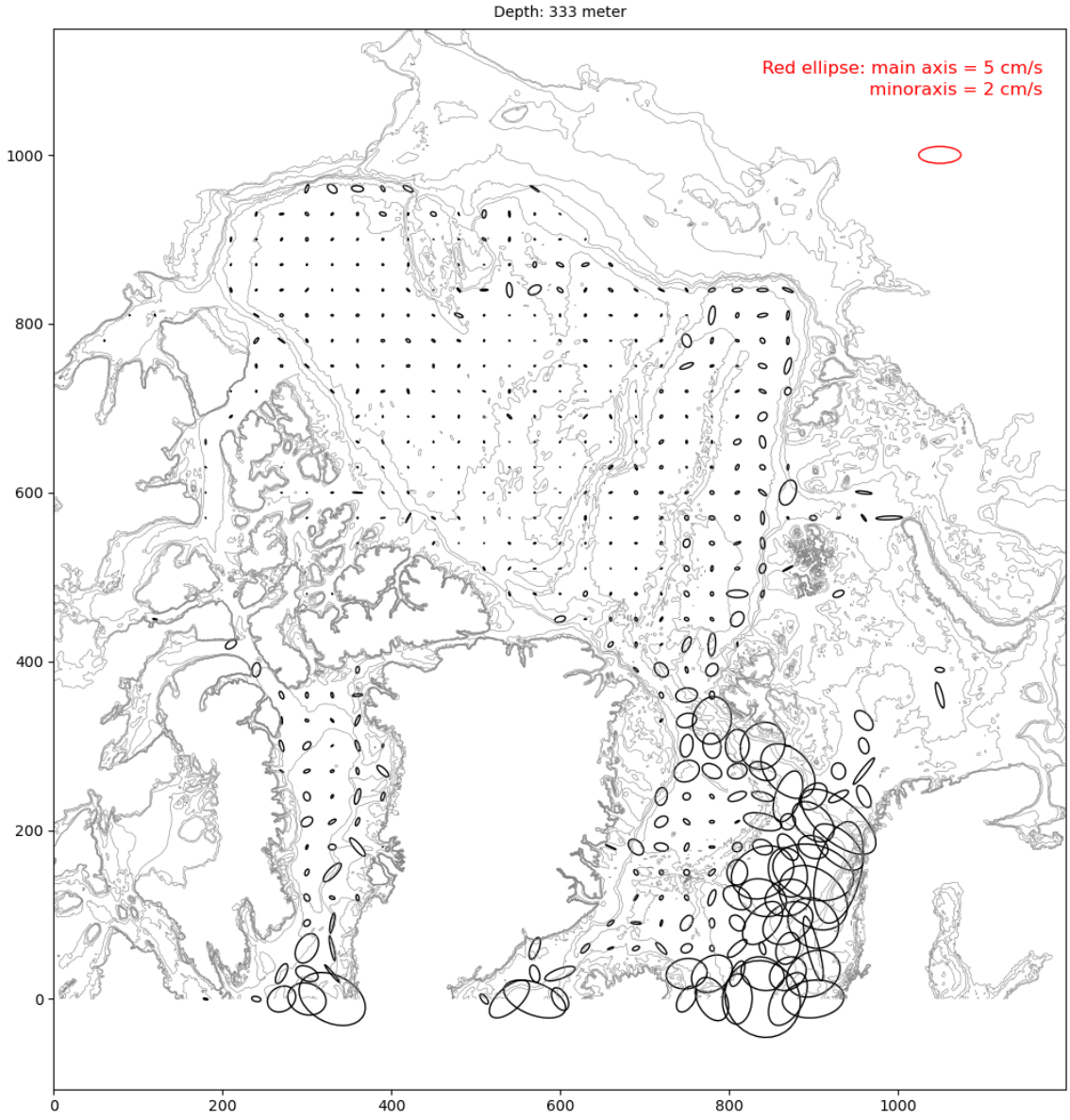

Figure 4.6: Horizontal variance ellipses for the current at 333 meters depth, in Arctic and sub-Arctic region. The main axis of the variance ellipse capture the majority of current direction, while minor axis capture the second largest portion of the current, orthogonal to the main axis. The size of the ellipses indicates the current strength. The variance ellipse marked in red is demonstrating the average current velocity, relative to the other ellipses. The strength of the red ellipse can be read in red to the upper right side.

minor axis, derived from EOF2, which is orthogonal to the dominant flow direction, is comparatively small and thus neglectable when drawing the ellipse. If so, the model data demonstrate zero or close to zero spread in the current directions for these locations. This is very unlikely in reality and can weaken the model's credibility. However, weak bottom flow is a known problem for numerical models in the Arctic Meneghello et al., 2021.

The model corresponds with previous observation (Timmermans and Marshall, 2020), exhibiting a velocity reduction with depth. The velocity and the variance have declined in strength for

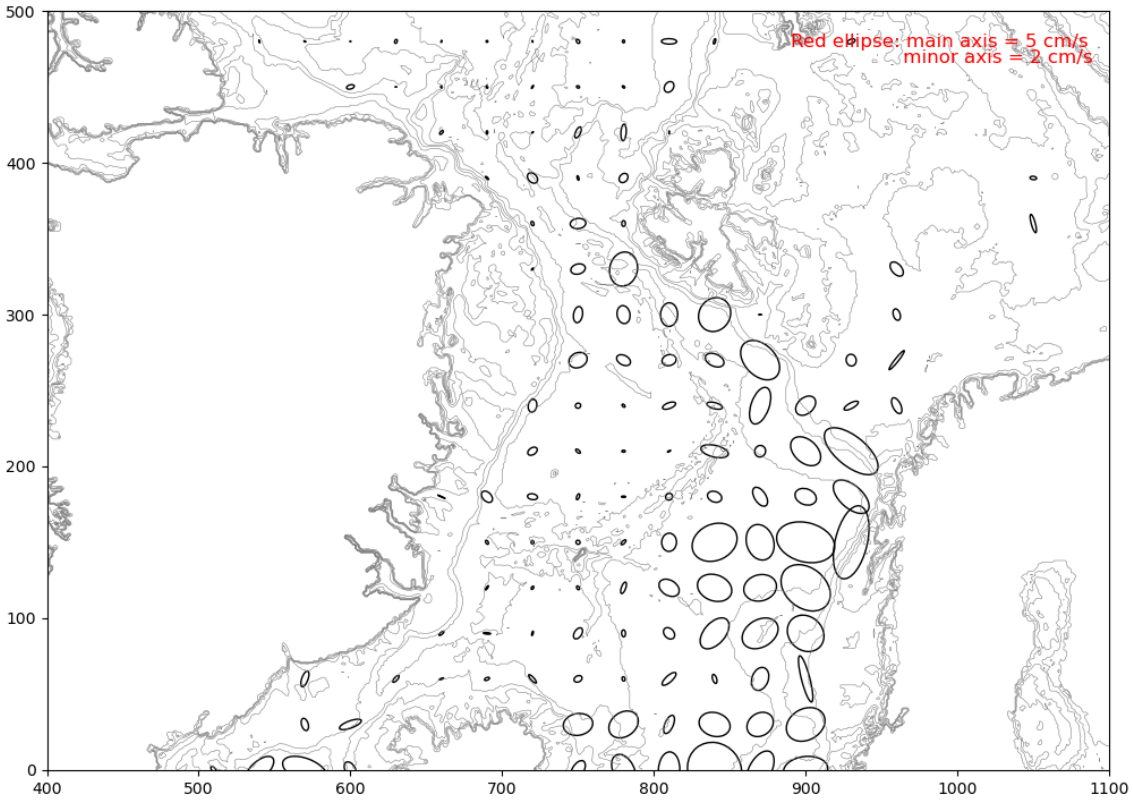

Figure 4.7: Horizontal variance ellipses for the current at 333 meters depth, zoomed in on the Norwegian coast. The main axis of the variance ellipse capture the majority of current direction, while minor axis capture the second largest portion of the current, orthogonal to the main axis. The size of the ellipses indicates the current strength. The variance ellipse marked in red is demonstrating the average current velocity, relative to the other ellipses. The strength of the red ellipse can be read in red to the upper right side.

each investigated level, revealing weaker fluctuations for the interior flow. Atmospheric conditions dominate the surface currents, as the model demonstrate a homogenous, anticyclone flow pattern consistent with the high pressure located above the Beaufort Sea. The variance is most significant where the velocity is vigorous or in shallow regions. Deeper into the ocean's interior, the flow becomes less homogeneous, and may reflect the variations in bottom topography more. The flow direction is oriented parallel to the topography for flow over steep topography as continental slopes. However, the flow direction is less distinct in the middle of the basin and appears more randomly. This may be explained by the rough bottom, where irregularities in the topography at each location

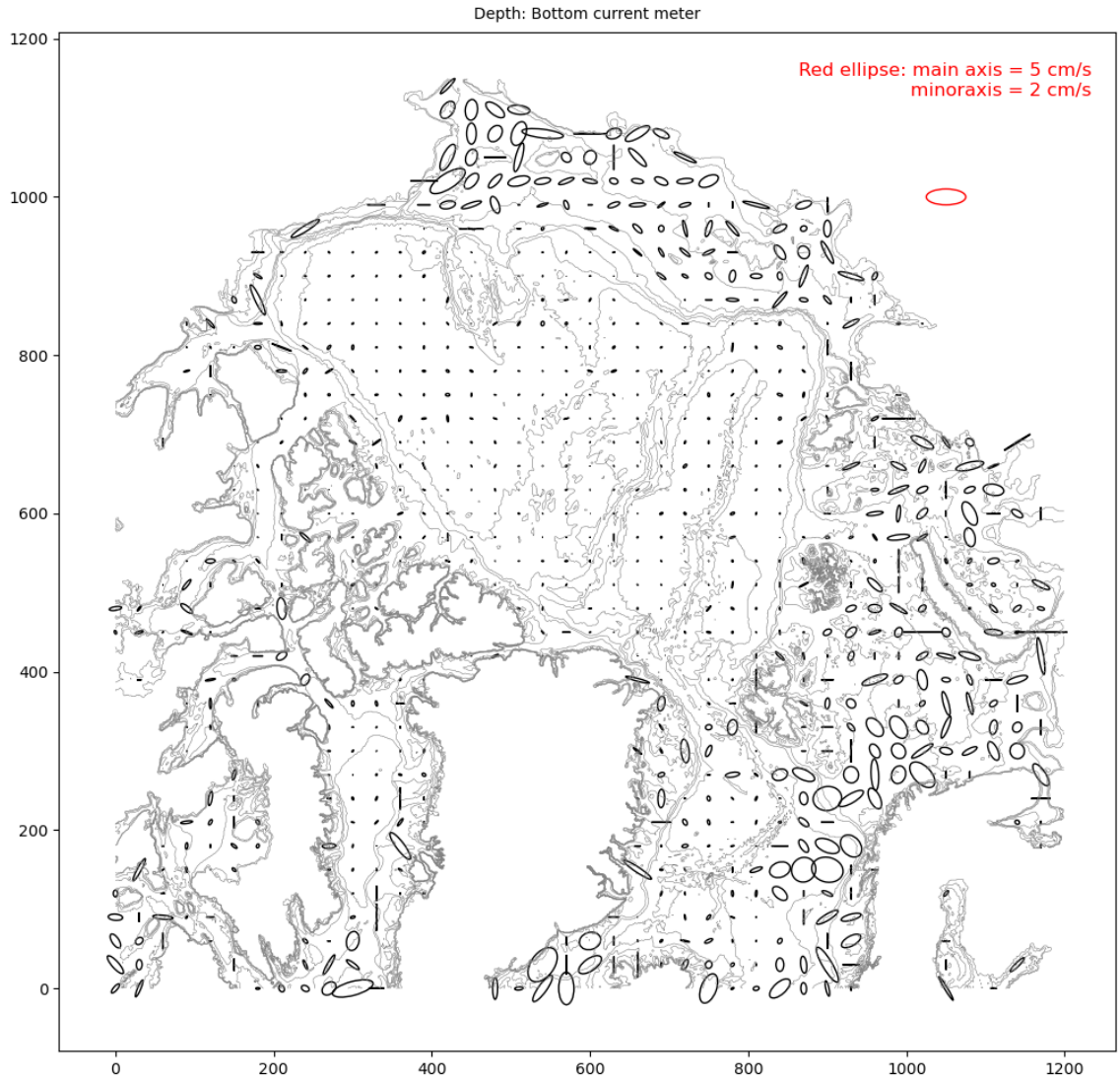

Figure 4.8: Horizontal variance ellipses for the bottom current, in Arctic and sub-Arctic region. The main axis of the variance ellipse capture the majority of current direction, while minor axis capture the second largest portion of the current, orthogonal to the main axis. The size of the ellipses indicates the current strength. The variance ellipse marked in red is demonstrating the average current velocity, relative to the other ellipses. The strength of the red ellipse can be read in red to the upper right side.

affect the current higher in the water column. A significant fraction of the bottom current is weak and close to zero.

4.2 Vertical structures at observation sites.

Empirical orthogonal functions (EOFs) are determined using principal component analysis (PCA) for observation and model data to investigate the vertical structure of the ocean currents. This thesis considers nineteen mooring records obtained from five locations and research groups. Three

mooring locations have greater depths than 1000 meters, while two are shallow, ≈100 meters deep. All mooring stations have a corresponding model station. In the following sections, EOFs will be referred to with the station name of the mooring, specifying whether the model or observation EOFs are evaluated when needed. As mentioned at the beginning of chapter four, section 4.1, the velocity records are rotated after EOF1 and EOF2, derived from the horizontal velocity at mid-depth, and normalized to conserve the amplitude to investigate if the extent of topography is steering performed in the Arctic. Thus, the degree of anisotropy in the current direction and orientation aligned with the topography indicates the amount of topographic steering felt by the currents. The horizontal variance ellipses used for rotation are visualized in Figure 4.9 and Figure 4.10, for the mooring and model data respectively. The variance ellipses are derived from the same depth for each mooring and model station. However, the evaluated depth may vary from station to station, as the station depth varies from merely 100 meters to over 2500 meters deep for others. Thus, a common reference depth is hard to determine. The horizontal variance ellipses for each station are estimated from an approximately mid-water column depth. The dot product between the velocity data and EOF1 to the horizontal variance ellipses derives the velocity parallel to the main flow, referred to as EOF parallel, $EOF_{||}$. For the velocity orthogonal to the main flow, referred to as EOF cross, $EOF_{\perp}$, EOF1 is rotated 90 degrees first.

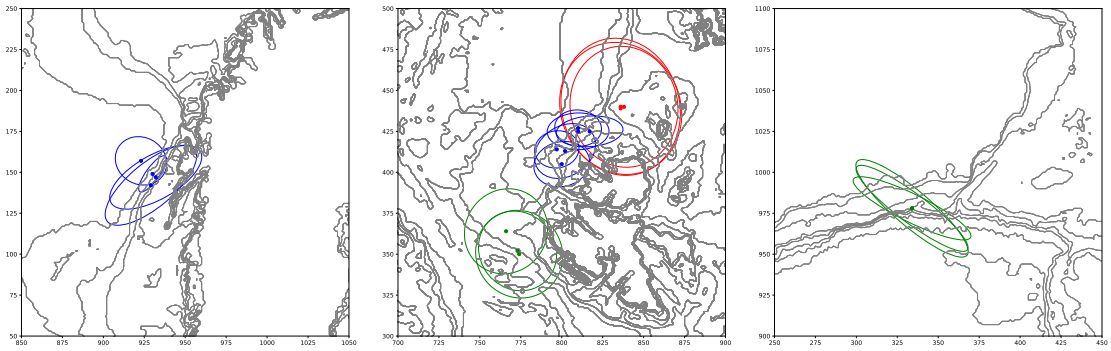

Figure 4.9: Horizontal variation ellipses derived from observation records. The Lofoten stations are visualized in the panel to the left. The mid panel demonstrates valiance ellipses derived from the Yermak Plateau in green, derived from the stations North of Svalbard in blue, and the stations from the Barents Sea are visualized in red. The variance ellipses derived from the Beaufort Sea are pictured in the right panel. The variation ellipses are used to rotate the velocity data in the main and minor axis direction.

The observation records are conducted between varying depths. Ranging from five meters below the surface to 200 meters below, all stopped before reaching the bottom. The observation EOFs are weak or zero from the first measurement, increasing downward to various extents. As discussed at the beginning of section 4, the demonstrated increase/decrease from the first measurement/towards the last measurement in the EOFs may result from substituting zeros for nan values in the observation records. The substituted zero-values decrease the average velocity and may dominate the variance, revealing a more significant decline than measured. The solution has been to derive the total variance estimated with depth to verify if the same decline is demonstrated. The total variance is constructed without nan values, thus having less bias. The total variance and the EOFs correlated strengthens the reliability of the EOFs. Thus, the EOF is believed to pick up a true signal. For the EOF and the total variance anti-correlated, is the signal believed to result from the zero substitution.

Both EOF1 and EOF2 have been estimated in this work, whereas only EOF1 is discussed further in the thesis. Except for the moorings located north of Svalbard, EOF2 reveal a percentage of variance explained (PVE) less than 26% for both model and observation data. Most of the EOF2 exhibit PVE less than 10%. Figure 4.11 displays EOF1 and EOF2 derived from the observation records deployed in Lofoten, visualized as a example of EOF2 for the observation data. For deeper

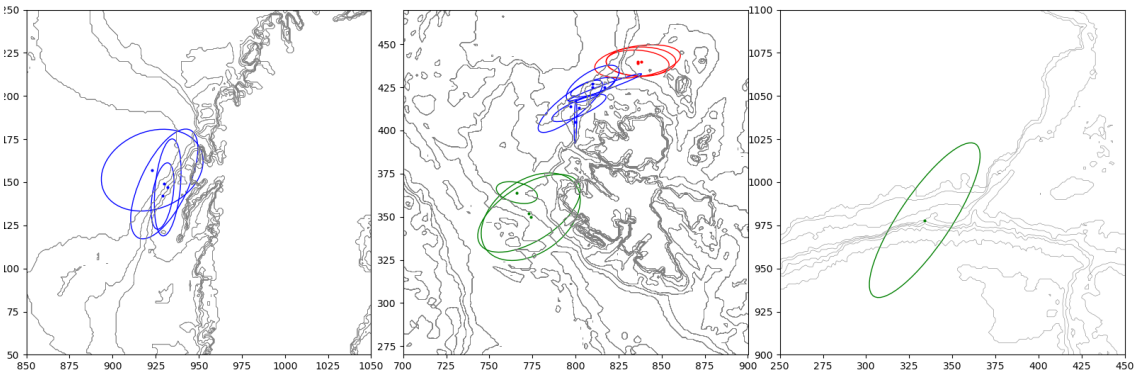

Figure 4.10: Horizontal variation ellipses derived from model data. The Figure illustrates the exact locations and the same colors as for the stations in Fig.4.9, only for the model data instead. The variation ellipses are again used to rotate the velocity data in the main and minor axis direction.

stations, as North of Svalbard, visualized in Fig.4.12, have EOF2 PVE≈25% for $EOF_{\perp}$ and PVE≈ 18% for $EOF_{||}$. The model EOF2 (not illustrated) demonstrates an even greater PVE for the same stations, <35%, which is a substantial fraction of the vertical structure. However, the model demonstrates the most significant fraction of the structure captured by EOF2, whereas for the observation data, only the two deepest stations demonstrate PVE≈24% for EOF2. Observation data is crucial for providing a representative result for the Arctic. Thus, as most of the vertical structures from the mooring records are captured by EOF1, this thesis will only discuss EOF1 further.

The observation records are also estimated for a five-days smoothed time series to obtain the same temporal resolution as the model data. However, as it does not demonstrate a significant difference from the original estimate, the five-days estimate is not visualized in any figures but may be discussed.

North of Svalbard

The stations deployed North of Svalbard are analyzed in the following section. The stations located to the East on the slope are visualized in Fig.4.13, and the stations to the West on the slope are visualized in Fig.4.14. The deepest station to the East, E3, is pictured to the left in Fig.4.13, E2 in the middle, and E1 (the shallowest East located station) to the right. The E3 station is the only observation EOF demonstrating zero crossing, where $EOF_{\perp}$ crosses zero at 900 meters and 1100 meters depth. However, the EOF is weaker below the zero-crossing more than in the opposite direction. Both EOFs are non-vanishing at the bottom, with $EOF_{||} > EOF_{\perp}$ throughout the rest of the water column. The EOFs increases from the first measurement, at ≈300 meters, demonstrating a peak at 500 meters depth. This incline is unsupported by the total variance estimated with depth, demonstrating the opposite trend. As mentioned at the beginning of section 4.1, is the total variance derived without substitution with zero for the nan-values. Thus, indicating a more accurate description of the recorded velocity in the beginning, as the EOFs contain zero values close to the first and last measurements. The total variance reveals a small bowl towards lower values for the last measurements. The slight increase at the bottom is interpreted as noise, as it is highly unrealistic.

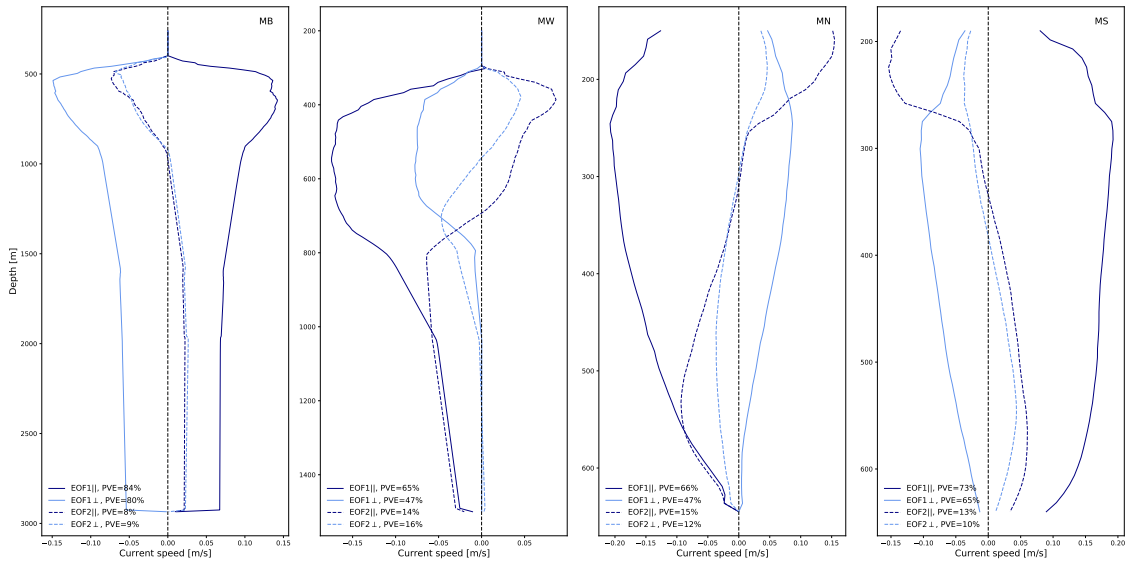

Figure 4.11: EOF1 (solid line) and EOF2 (stippled line) derived from observation records obtained from Lofoten, rotated along and across EOF1 derived from the horizontal currents for each station. The basin mooring, MB, is visualized to the left, followed by MW (the West mooring), MN (the North mooring) and MS (the South mooring) to the right.

The West located deep station, W3, depicted to the left in Fig.4.14 is similar to the corresponding East station, E3, for both $EOFs_{||}$ and $EOF_{\perp}$. However, W3 does not cross zero but decays more smoothly with depth. A comparable structure may be anticipated for the two stations as they are adjacent and approximately the same depth. The W3 station exhibits $EOF_{||} \approx EOF_{\perp}$, whereas the E3 station $EOF_{||} > EOF_{\perp}$. The total variance demonstrates a decrease from the first measurement again, suggesting the dampened EOF signal at the top for both stations may be incorrect. W3 demonstrates larger PVE, thus capturing a more considerable percentage of the vertical structure.

The stations deployed North of Svalbard are visualized in the mid panel, blue ellipses for Fig.4.9. The ellipses to the left correspond to the West located stations demonstrating isotropy. The ellipses to the right correspond to the East located stations and demonstrate anisotropic variance with a cross slope orientation. The asymmetrical orientation is also shown for the vertical structure. The East located stations display $EOF_{||} > EOF_{\perp}$, whereas the West stations have $EOF_{||} \sim EOF_{\perp}$. The East stations are located closer to the Barents Sea opening, where cold water from the Barents Sea enters the Arctic along the isobaths on the east side of Svalbard. Thus, maintaining a cross slope direction. On the other hand, the stations located to the West are further away from the opening, where the isobaths bend westward, guiding the flow along the topography.

The four remaining moorings station North of Svalbard exhibit EOFs decaying smoothly, with a peak close to the first measurement and PVE>70%. The corresponding East and West stations depict similar EOF structures for all stations. The total variance estimated with depth and the EOFs depicts an increase with depth at the beginning. Thus, the two structures are agreeing. However, the agreement is weaker for the two shallowest stations, E1 and W1, as the decline is not as significant. For W1, it may even appear depth-independent.

The practical salinity and potential density derived from the observation data are visualized in Fig.4.15. The two deepest stations are furthest to the left, with East 3 first and West 3 to the second left, followed by East 2 and West 2 in the center, and East 1 to the right, as West 1 is missing. The stations demonstrate approximately uniform density initially, followed by a sharp pycnocline. The pycnocline varies in scale and extent. The E3 station exhibit the sharpest pycnocline. For the two deeper stations, E3 and W3, the EOFs peak below the pycnocline. Conversely, the shallower

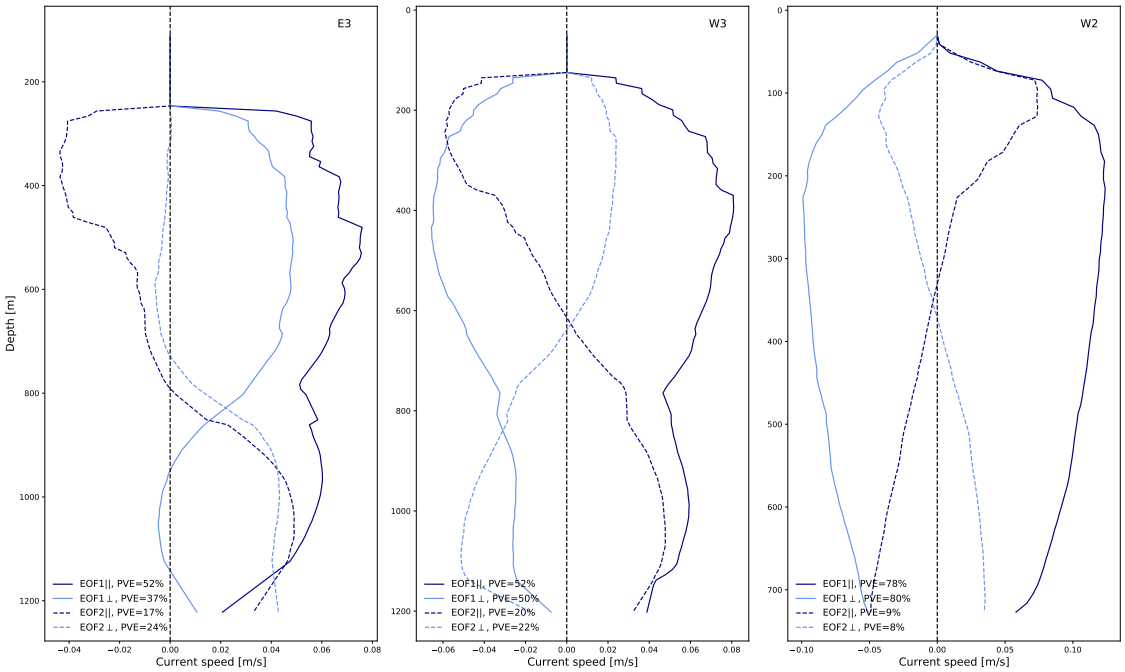

Figure 4.12: EOF1 (solid line) and EOF2 (stippled line) derived from observation records obtained North of Svalbard, rotated along and across EOF1 derived from the horizontal currents for each station. The deep East mooring, E3, is visualized to the left, followed by the deep west mooring, W3, and to the right the second deep West mooring, W2.

stations demonstrate a peak in the EOFs for depths equivalent to the beginning of the pycnocline.

The EOF derived from model data demonstrates a weak surface signal and $EOF_{||} > EOF_{\perp}$. The velocity is significantly underestimated for the whole water column. $EOF_{||}$ increases with depth, demonstrating a subsurface maximum. $EOF_{\perp}$ decreases from the surface, reaching zero at shallower depths. All model EOFs depict zero or close to zero bottom velocity. The two deeper model stations located to the West, W3, and W2, display zero-crossing higher in the water column. The shallower station, W2, reveals more weak flow than the opposite flow above the zero crossing, thus may not be that accurately captured. For the deeper station, W3 is the zero-crossing more distinct. The horizontal variance ellipses from model data are visualized in Fig.4.10, again blue ellipses, mid-panel. The variance ellipses illustrate significantly greater anisotropy.

Lofoten, basin and slope

The second deep station area is from Lofoten, visualized in Fig.4.16. The deepest station is the basin mooring, MB, visualized to the left in Fig.4.16. The MB station is located away from steep topography and displays isotropic variance, shown in Figure 4.9, the left panel. Compliance with this is $EOF_{||} \approx EOF_{\perp}$. The EOFs display a distinct peak at 500 meters and become uniform with a depth below 700 meters. Again, the EOFs reveal a decrease towards the first measurement, supported by a similar decay for the total variance. This tendency repeats for all the Lofoten stations. Thus, encouraging the hypothesis that the amplitude reduces as depth decreases. The station located to the West on the slope, MW, is the second deepest mooring station in Lofoten. The structure resembles the MB-EOFs, only with $EOF_{||} > EOF_{\perp}$. Thus, experience more potent topographic steering as the variance ellipses is parallel to the isobaths in Fig.4.9. $EOF_{\perp}$ vanish from 700 meters.

The variance ellipse used for rotation, shown in the first panel in Fig.4.9, implies greatly anisotropic

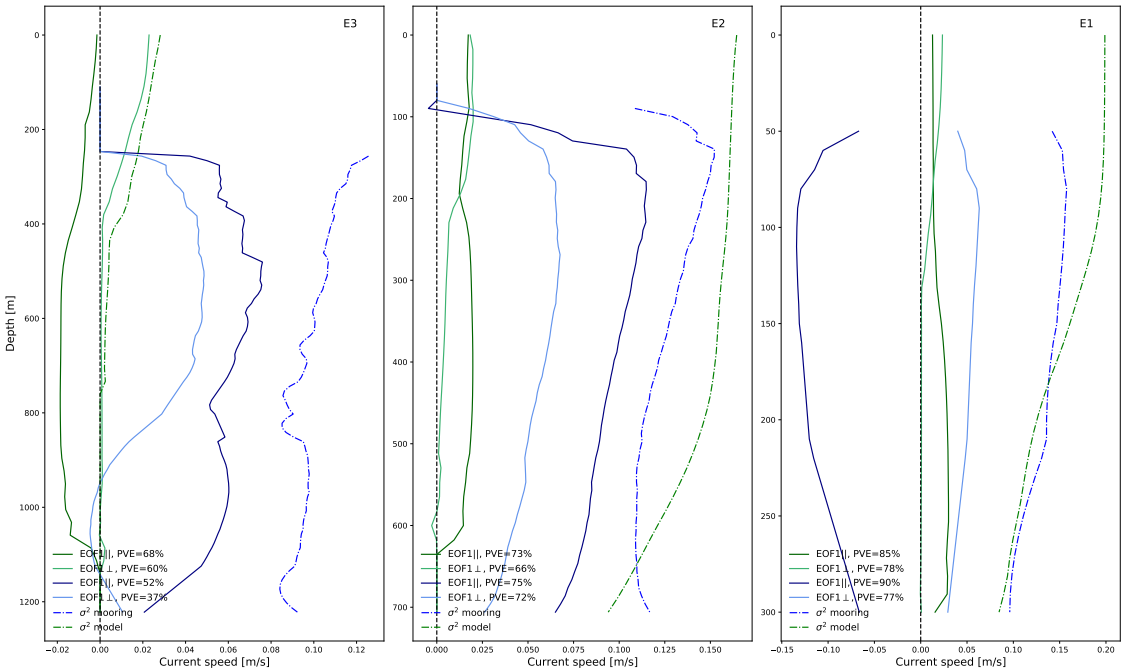

Figure 4.13: EOF1 (solid line) and the total variance with depth (stippled with dots line) derived from model and observation data North of Svalbard, located to the East on the slope. The model EOFs and total variance estimated with depth are visualized in green colors, whereas the observation EOFs and total variance estimated with depth are visualized in blue colors. Both model and observation EOFs are rotated along and across EOF1 derived from the horizontal velocities for each station. The deep East located mooring, E3, is visualized to the left, followed by the second deep mooring, E2, and the shallowest East located mooring, E2, to the right.

variance, with orientation along the isobaths for all the three stations over the slope. The basin station, however, located over flat topography, demonstrates an isotropic variance. This is confirmed by the EOFs as all stations, except the MB station, exhibit $EOF_{||}$>$EOF_{\perp}$. Hence, the results agree with previous expectations that topographic steering occurs over steep terrain as variations in the Coriolis parameter can not compensate for changes in depth.

The MN and the MS stations are shown second furthest and furthest to the right. Both stations demonstrate a peak at shallower depth, decreasing above and with a smooth decay towards the bottom below. For the MN-station, the EOFs approach zero at the bottom, whereas is non vanishing for the MS-station. Both stations demonstrate corresponding decay for the EOFs and the total variance towards the first measurement. However, the decay is more significant for the EOFs than the total variance. Thus the weak amplitude, in the beginning, might be too drastic.

The practical salinity obtained from the Lofoten stations and the derived potential density is visualized in Fig., with the MB station to the left, MW station in the middle, and MN station to the right (MS is missing). The two deeper stations, MB and MW, demonstrate the EOF maximum in the pycnocline. Conversely, the MN station demonstrates a maximum below the pycnocline.

The EOFs derived from model data display a maximum for MB and MW stations at the surface. The basin mooring, MB, is close to uniform from the surface, revealing a decay first at 2000 meters depth. The MW station is again resemble the MB station with $EOF_{||}$>$EOF_{\perp}$. However, the model exhibits a more rapid decay than the observation EOF, reaching zero velocity at the bottom for both EOFs. For the two lateral stations, the model EOFs agree with the observation more. The EOFs decay smoothly with depth at both stations, approaching zero at the bottom.

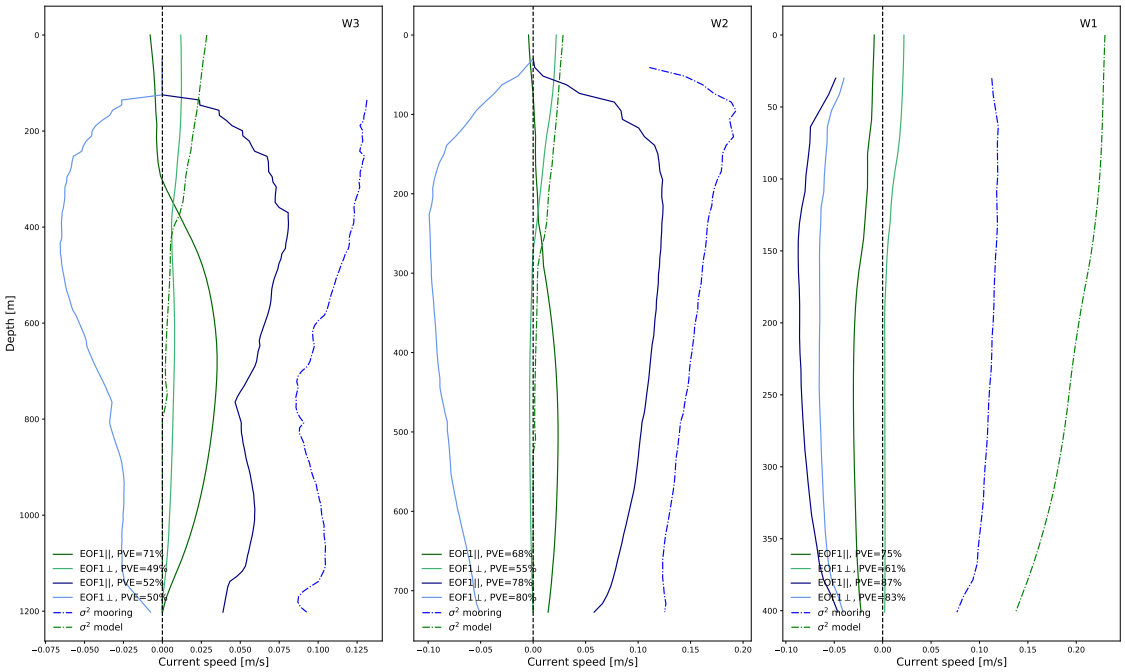

Figure 4.14: EOF1 (solid line) and the total variance with depth (stippled with dots line) derived from model and observation data North of Svalbard, located to the West on the slope. The model EOFs and total variance estimated with depth are visualized in green colors, whereas the observation EOFs and total variance estimated with depth are visualized in blue colors. Both model and observation EOFs are rotated along and across EOF1 derived from the horizontal velocities for each station. The deep West located mooring, W3, is visualized to the left, followed by the second deep mooring, W2, and the shallowest West located mooring, W2, to the right.

Yermak Plateau

Yermak plateau is the last region with deeper moorings, visualized in Fig.4.18. All three stations exhibit a peak close to the first measurement. Y1, pictured to the left in Fig.4.18, reveal a more substantial decline for the EOFs, becoming close to zero at the bottom. The total variance illustrates a subtle increase from 700 meters, suggesting the EOFs capture the variance higher in the water column better, as the total variance and the EOF agree more. The two remaining stations, Y3 visualized in the middle and Y2 to the right in Fig.4.18 are more similar again, exhibiting non-vanishing EOF at the bottom and close to uniform with depth. Y2, located on the plateau, demonstrate $EOF_{||} \approx EOF_{\perp}$. The total variance agree with the fast decline close to the first measurement for all three stations, indicating a dampened signal fro the EOFs higher in the water column. The horizontal variance ellipses from Yermak Plateau visualized in Fig.4.9 revile essentially isotropic current direction for the observation data, agreeing with the $EOF_{||} \approx EOF_{\perp}$.

The two deeper stations, Y1 and Y3, demonstrate deep maximums for the model EOFs, at 800 meters depth. Both EOFs become zero at the bottom. The Y2 model station, located on the plateau, displays a slight rise/dip for $EOF_{||}/EOF_{\perp}$ respectively, at$\sim$ 200 meters depth, with $EOF_{||}>EOF_{\perp}$. The EOFs approach zero near the bottom. The horizontal variance ellipses from the model station confirm the anisotropy demonstrated by the EOF.

Beaufort shelf and the Barents Sea

The observation records obtained from Beaufort sea were unfortunately poorly captured, with more than 2/3 of the water column lacking from the data for the 2014 and 2016 moorings. Furthermore

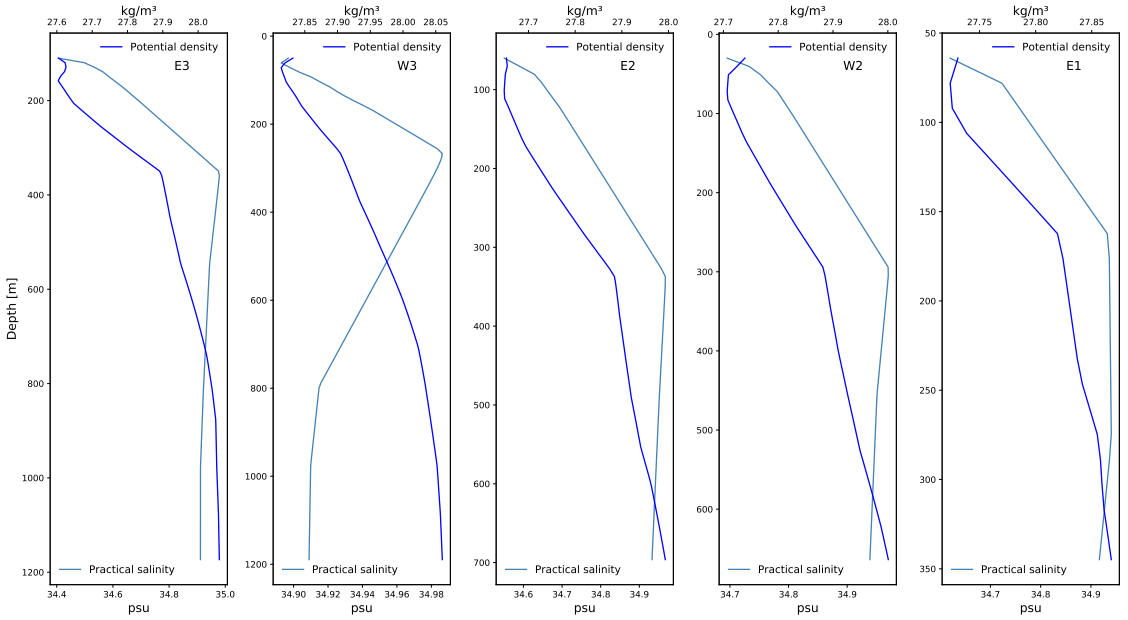

Figure 4.15: Practical salinity obtained from observation records (steel blue) located North of Svalbard, and the potential density (grey) derived from the respective salinity and temperature measurements. The deep East station, E3, is visualized to the left, followed by W3, E2, W2, and E1 visualized furthest to the right (W1 was lacking salinity data).

demonstrates the 2018 mooring gaps where measurements are not excising. Thus, good evaluations and characteristics are challenging to determine. However, as actual observations are rear and essential when concluding something about the real world, are the mooring records preserved and discussed to the best ability.

Both the Beaufort and the Barents Sea are shallow, thus not as representative for the Arctic, predominantly of greater depths. Hence, the figures are not visualized, but can be found in the appendix A. The EOFs will henceforth only be discussed briefly. The surface and bottom velocity are approximately of the same strength at both locations. Thus, the EOFs are close to uniform with depth, with a slight slope. For the model EOFs are the structures quite different. The Barents Sea reveal surface intensification, with both EOFs vanishing at mid depth. For the Beaufort Sea, the EOFs are close to uniform from the surface, revealing a rise/dip close to the bottom. Non of the observation EOFs agree with the model structure.

4.3 The role of sea ice

The numerical ocean model is applied to explore further the dynamical features of sea ice cover and flat and sloping bottom topography on the vertical structure. The aim is to investigate if the observation data findings are broadly applicable to the entire ice-covered Arctic Ocean. Notably, the findings in section 4.2, comparing the observation data and model data, indicated that the model performance might not be good enough to produce reliable information. However, the CREG12 simulation is further investigated in the absence of a better model.

Eight additional EOF are produced from the model data. Three EOFs are derived from ice-free model regions, whereas five are derived from regions covered by sea ice. The aim is to distinguish if different characteristics dominate the vertical structure for EOFs derived from different dynamical conditions. Thus, to determine the impact of sea ice, if any, on the vertical structure.

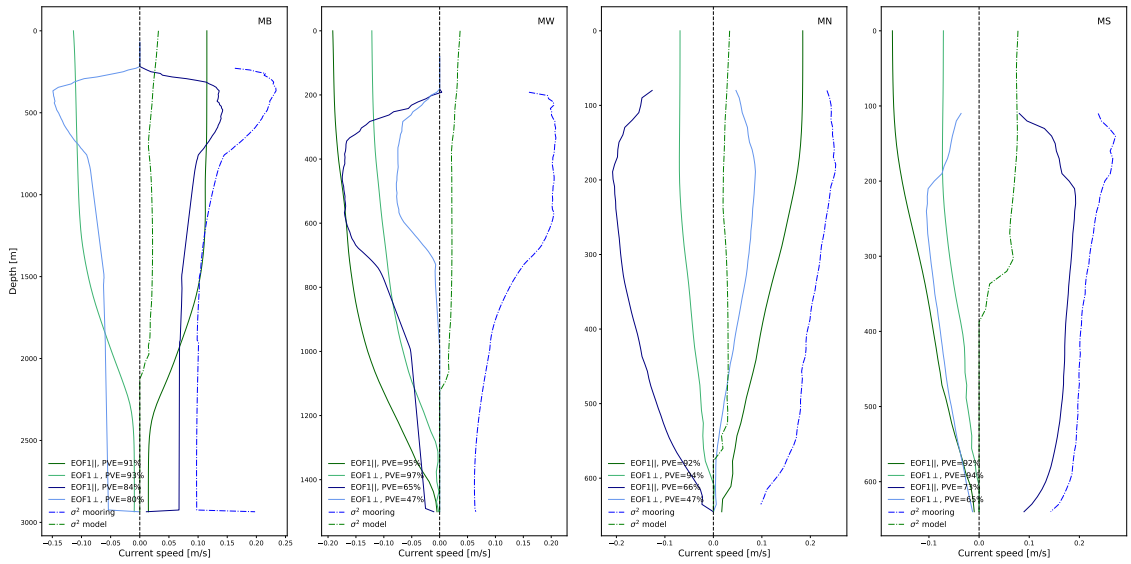

Figure 4.16: EOF1 (solid line) and the total variance with depth (stippled with dots line) derived from model and observation data obtained from Lofoten. The model EOFs and total variance estimated with depth are visualized in green colors, whereas the observation EOFs and total variance estimated with depth are visualized in blue colors. Both model and observation EOFs are rotated along and across EOF1 derived from the horizontal velocities for each station. The deep basin mooring, MB, is visualized to the left, followed by the MW mooring (located to the West), the MN mooring (located to the North), and the MS mooring (located to the South) visualized to the right.

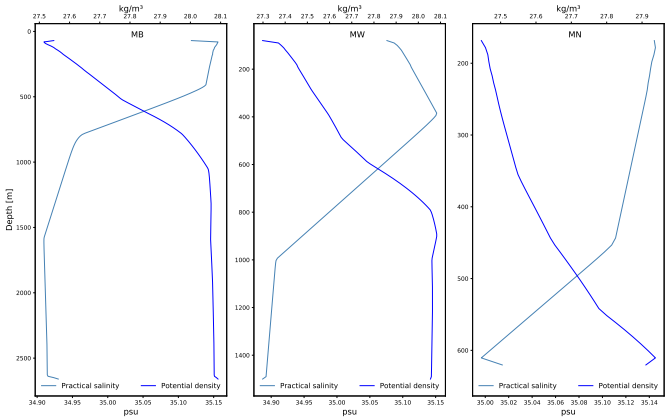

Figure 4.17: Practical salinity obtained from observation records (steel blue) located in Lofoten, and the potential density (grey) derived from the respective salinity and temperature measurements. The deep basin station, MB, is visualized to the left, followed by MW (to the West), and MN (to the North) to the right (MS is missing).

Ice free regions

Figure 4.21 displays the calculated EOFs derived from ice-free regions over steep topography. The EOF to the left in Fig.4.21 is derived from outside Stad in Møre and Romsdal. The mid-EOF is derived South of Svalbard, and the EOF to the right from South of Jan Mayen. All three stations demonstrate the same structure, revealing a maximum at the surface, becoming zero or close to zero at the bottom. All station have $EOF_{||} > EOF_{\perp}$. However, the EOFs south of Jan Mayen

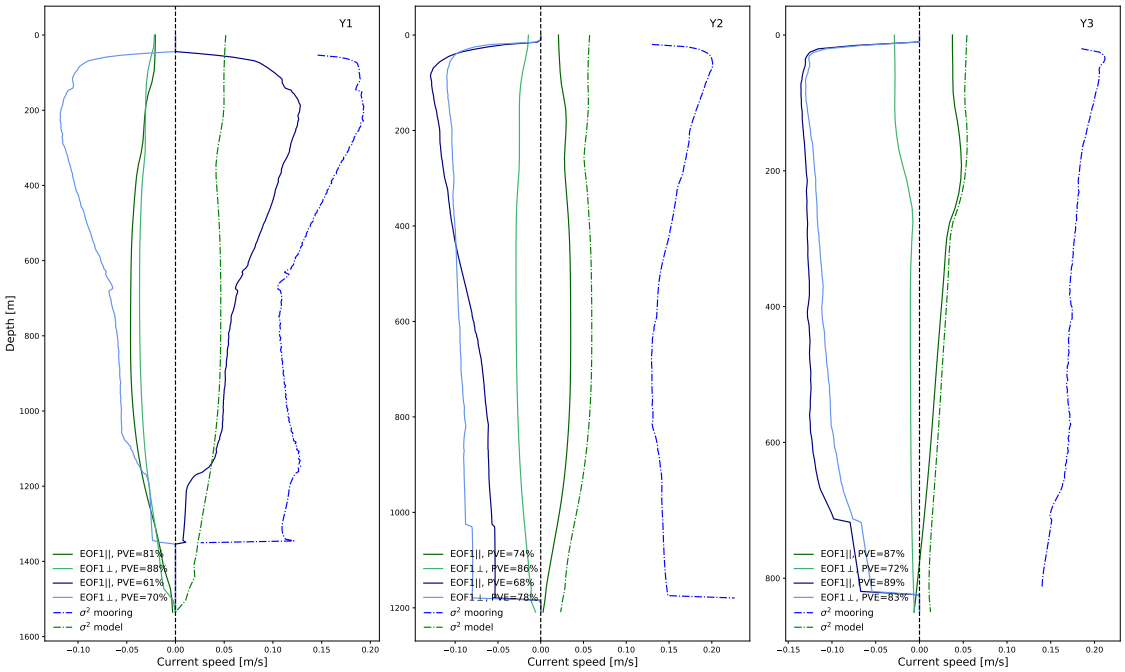

Figure 4.18: EOF1 (solid line) and the total variance with depth (stippled with dots line) derived from model and observation data obtained from Yermak Plateau. The model EOFs and total variance estimated with depth are visualized in green colors, whereas the observation EOFs and total variance estimated with depth are visualized in blue colors. Both model and observation EOFs are rotated along and across EOF1 derived from the horizontal velocities for each station. The deep mooring, Y1, is visualized to the left, the second deep station, Y3, in the middle, and the shallow station, Y2, to the right.

reveal a weaker velocity. All stations show high PVE>77% and with a total variance resembling the dominant EOF, $EOF_{||}$.

Sea ice regions over steep terrain

The EOFs calculated from regions experiencing sea ice cover, located over steep terrain, are visualized in Fig.4.22. EOF derived from the East part of the Barents Sea towards the Nansen basin is visualized to the left. EOF derived from the Laptev Sea is visualized in the middle and to the right from the continental slope close to Canada.

$EOF_{||}$ crosses $EOF_{\perp}$ two times for the Barents Sea station. First close to the surface, then later close to the bottom, revealing a peek at mid-depth. The zero-crossing close to the bottom for $EOF_{||}$ is believed to be a numerical error. None of the other model EOFs indicate a similar crossing or decay close to the bottom. Both EOF exhibits large PVE>69%.

The EOF derived from the continental slope in the Laptev Sea is visualized in the mid panel Fig.4.22. The EOFs demonstrate maximum at the surface for both EOFs. $EOF_{\perp}$, with PVE=81%, demonstrate a severe decay from the surface, becoming zero close to the surface. $EOF_{||}$ reveals a dip from the surface, illustrating a maximum at 100 meters depth. $EOF_{||}$ is non-vanishing a the bottom.

The last EOFs from ice-covered regions over sloping topography are located over the continental slope close to Canada. Both EOFs have a maximum at the surface, decaying towards the bottom. $EOF_{\perp}$ (PVE=77%) resembles $EOF_{\perp}$ from the Laptev Sea, becoming zero close to the surface.

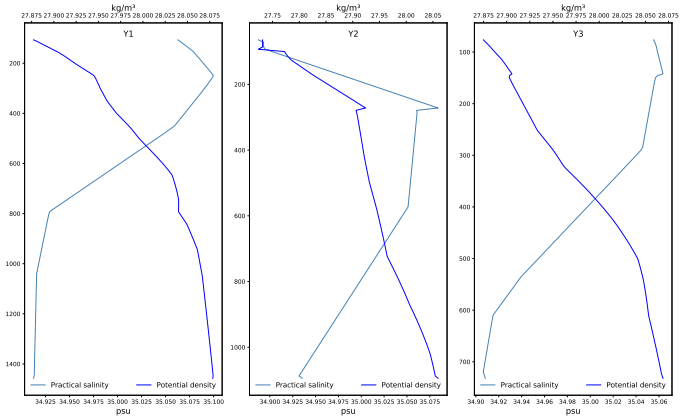

Figure 4.19: Practical salinity obtained from observation records (steel blue) located Yermak Plateau, and the potential density derived from the respective salinity and temperature measurements. The deepest station, Y1, is visualized to the left, followed by Y3, and Y3 (located more on the plateau) visualized to the right.

$EOF_{||}$ (PVE=80%) decay from the surface, revealing a maximum deeper in the water column at 400 meters. $EOF_{||}$ becomes small close to the bottom.

Sea ice regions over flat or rough terrain

The last two EOFs calculated from model data solemnly are visualized in Fig.4.23 and are from regions experiencing sea ice located over the flat or rough topography. The EOFs in the left panel are derived from the Makarov Basin, and the EOFs to the right from the Bering Sea. Both EOFs are surface intensified, becoming approximately zero from 160 meters depth, with $EOF_{\perp} \sim EOF_{||}$. This corresponds to the expectation that stations over flat terrain have no favorable direction, thus isotropic variance. Both stations show a rise in the total variance between 60-140 meters.

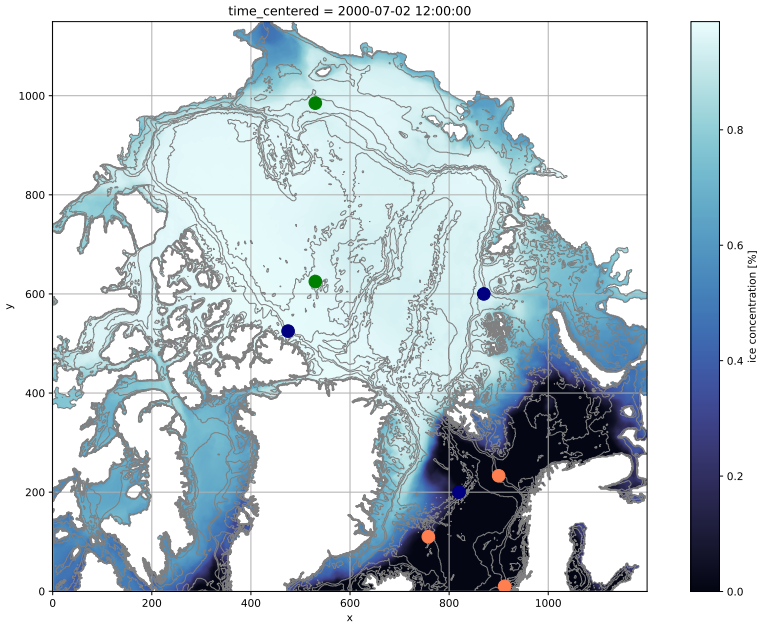

Figure 4.20: Map showing the sea ice cover and ice thickens for the model data.The ice thickness can be read from the scale to the right. The different dot is visualising where the model EOFs are calculated from, where the peach color indication ice free EOFs, the blue ones are form ice cover regions over steep topography and the green dots are EOFs from ice covered regions over flat topography.

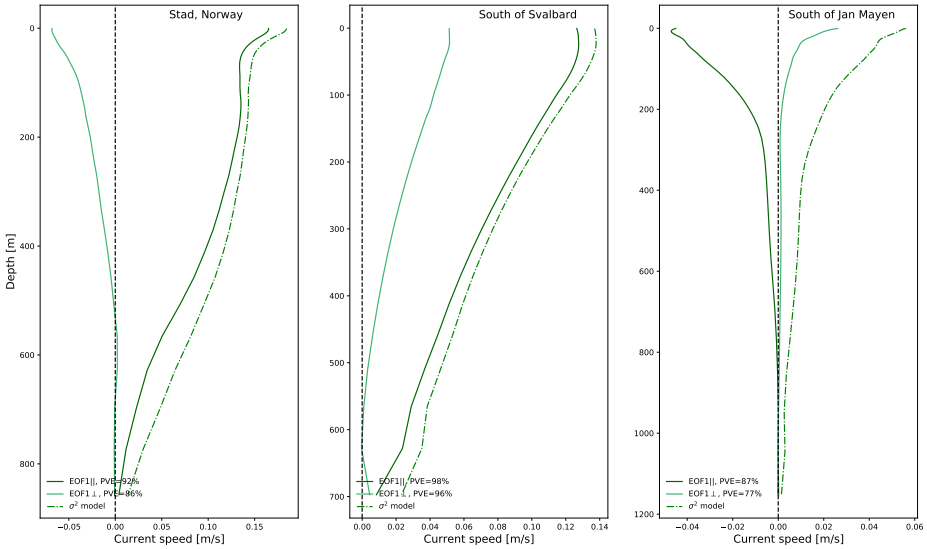

Figure 4.21: EOF1 and the total variance with depth calculated from model data solemnly, rotated along and cross mean velocity for each station, in ice free regions. The EOF to the left is calculated from outside stad on the slope, the mid EOF are calculated from south of Svalbard on the continental slope, and the EOF to the right are calculated form south of Jan Mayen.

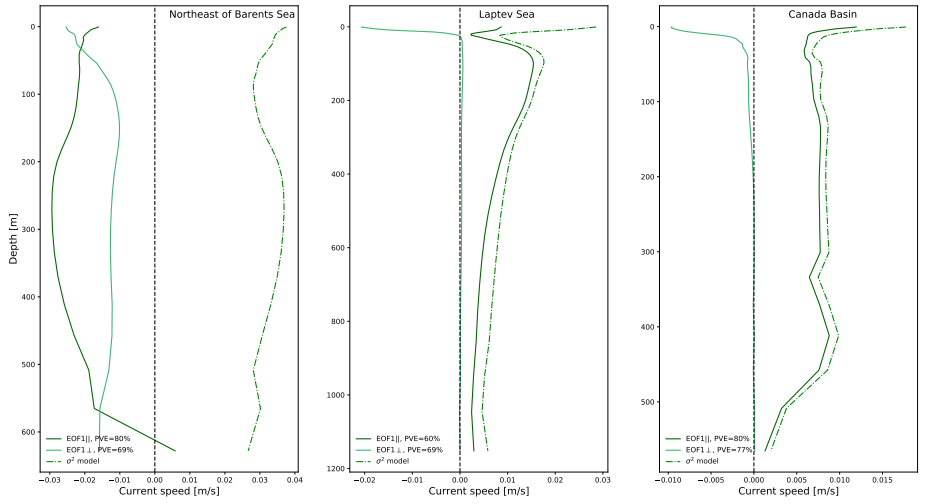

Figure 4.22: EOF1 and the total variance with depth calculated from model data solemnly, rotated along and cross mean velocity for each station, in ice covered regions over steep topography. The EOF to the left is calculated from east part of the Barents sea on the slope towards Nansen basin, the mid EOF are calculated from over the continental slope in Laptev sea, and the EOF to the right are calculated form over the continental slope close to Canada.

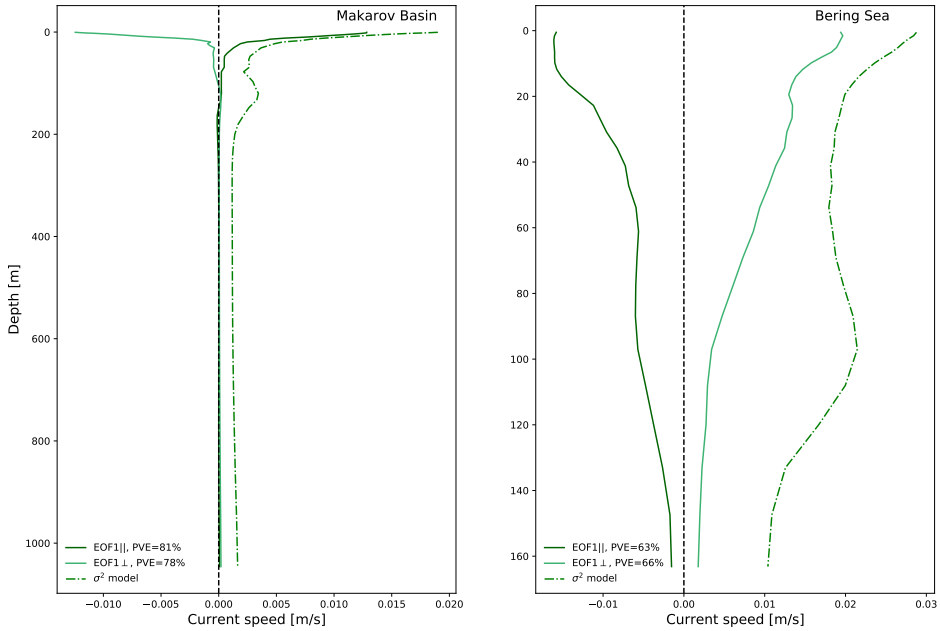

Figure 4.23: EOF1 and the total variance with depth calculated from model data solemnly, rotated along and cross mean velocity for each station, in ice covered regions, over flat topography. The EOF to the left is calculated from Makarov basin, and the EOF to the right is calculated form the Bering sea.

CHAPTER 5

Discussion and Conclusion

Nineteen empirical orthogonal functions (EOFs) are analyzed, derived from moorings deployed in the Arctic and sub-Arctic regions from various projects and years. The records cover varying depths from 15 meters beneath the surface for shallower moorings to 300 meters beneath the surface for deeper ones. A lot of the surface and subsurface information is missing for the deeper moorings. Hence, conclusions regarding the entire vertical structure are difficult to make. A more significant fraction of the water column is represented for shallower moorings. However, the shallower moorings are not representative of the Arctic Ocean, featuring predominantly greater depths. Therefore, to conclude anything of confidence regarding the vertical structure of the Arctic and sub-Arctic region is complicated.

The observation EOFs increase in magnitude from the top measurement to various extents, depending on the station's depth. When constructing the EOFs, measuring errors where data is not provided (referred to as missing values or nan-values) were substitutes with zero, as the computation of the EOFs can not operate any missing values. Thus, the EOFs may be misguided for levels containing missing values, primarily close to the top and bottom of the station's vertical range. Therefore, the total variance, which can be constructed by removing the missing values, is derived to assess the validity of the EOFs. For the EOFs and total variance agreeing, hence decreasing/increasing with each other, the EOFs are validated. However, when the EOF and the total variance do not agree, hence one decreases as the other increases, the EOFs are invalidated. Thus, for invalidated EOFs, the reduction close to the top and bottom measurements is believed to result from substituting missing values with zero.

Most of the total variance estimated with depth demonstrated the same increase from the first measurement as the observation EOFs. Nevertheless, because the total variance does not include levels yielding only missing data points, it depicts a more precise line for where the data sets information ends, and the EOFs further illustrate substitution with zero. Four stations from the research project North of Svalbard expose a conflicting signal between the total variance and the EOF at the top measurements. The total variance and the EOFs reveal an opposite trend for the two deeper stations. Thus, the actual variance is assumed to increase further toward shallower depths. However, the compliance is marginal between the EOF and the total variance for the two remaining stations, raising a question mark as to whether the actual variance declines towards the surface. For the remaining 15 stations, the initial increase is assumed valid as the total vaiance and the EOFs agree, indicating reduced variance approaching shallower depths.

A more significant fraction of the surface layer is included for the shallower moorings. Thus the decay near the surface could be related to the sea ice cover, dampening the eddy fields at the surface. Meneghello et al., 2021 purposed that the surface intensification in the eddy field is anti-correlated with the thickness of the sea ice cover, dissipating exciting eddies and preventing the growth of new ones. This theory would be interesting to investigate further, as most of the moorings, except the Lofoten stations, are expected to experience sea ice cover. However, as the moorings lack data at the surface and bottom, the theory is difficult to evaluate further. Nevertheless, the total variance confirms the decay towards shallower depths for almost all the stations (exceptions mentioned

above). Thus, a mechanism reducing the eddy activity at a shallower depth is anticipated to be present. It is, however, difficult to identify the cause, as the velocity reduction near the top measurements is visible in all observation records, regardless of the depth and location.

The model performs pleasingly for the horizontal circulation pattern. The surface circulation displays the same pattern as observations, dominated by the wind regimes with high pressure over the Beaufort Sea, causing anticyclone flow in the Canadian Basin and southwestward flow in the Eurasian Basin. Aligned with the continental slope of the Eurasian Basin and especially along with the East parts of the Nansen Basin is a cyclone compensation current visible in the opposite direction of the rest of the basin. The model demonstrates a strong correlation between the current direction and the isobaths along the boundaries, thus indicating topographic steering. Furthermore, both the flow strength and the variance reduces for increased water depth and deeper flow in the water column, consistent with expectations. Increased variance on the continental slope from the shelf region is visualized in the figures zoomed in on the Norwegian Sea.

5.1 Interpretations in terms of baroclinic modes

As mentioned in the introduction, the periods of Rossby waves are long in the Arctic. Consequently, a year's duration is too brief to capture fluctuations of baroclinic Rossby waves. Nevertheless, in the absence of a more suitable theory, the EOFs will still be interpreted in terms of baroclinic modes obtained with 'rough' and 'flat' boundary conditions.

BC mode

The classical BC1 mode, calculated with a 'flat bottom' boundary condition, does not resemble most of the EOFs derived from observation records, as only one EOF exhibits zero-crossing. $EOF_{\perp}$ derived from observation data located to the East on the slope North of Svalbard, E3, crosses zero twice at greater depth. Accordingly, the 'flat bottom' BC2 should be the best option as the EOF is non-zero at the bottom. However, the zero-crossing is at profound depth and reveals a relatively weak velocity more than in the opposite direction after the crossing. The corresponding West located station, W3, displays a similar structure without the zero-crossing. A similar structure is anticipated as the two stations are adjacent and at the same depth. Thus, assuming the E3 station is incorrectly captured at depths, the 'rough bottom' BC1 is a more appropriate comparison, as the EOFs become weak at the bottom.

The EOFs do not comply with any known analytical vertical structures, making comparison difficult. Previously studies of the vertical structure indicate the primary EOF from current meter observations closely resembles the first baroclinic mode calculated with 'rough bottom' as the velocity tends to vanish at the boundary (La Lama et al., 2016, LaCasce, 2017). However, non of the stations investigated in this study reveal vanishing EOF at the bottom and thus, do not satisfy the conditions for the 'rough bottom' BC mode. A further comparison to the baroclinic null mode derived with the 'flat bottom' boundary condition provides BT mode, which is uniform with depth. Some stations may fit a BT description as they appear close to depth-independent. For example, the shallow stations from the Barents Sea reveal the same magnitude for the top and bottom measurements, suggesting a uniform decay. Nevertheless, the stations depict a maximum deeper in the water column and thus are not uniform. Also, the Yermak station, located on the plateau, suggests a uniform decay. However, the EOF reveals a decay approaching the boundaries. The total variance confirms the reduction, illustrating a slight increase from the top measurements before decreasing towards the bottom. Finally, the basin mooring in Lofoten might also demonstrate a close resemblance to the BT mode. The EOF is roughly uniform for a significant fraction of the vertical measurement, supported by the total variance. However, the station depicts a distinct peak close to the top measurement, which the BT mode can not explain. Hence, in conclusion, non of the stations discussed above satisfies a uniform BT mode, implying the 'rough bottom' BC1 mode may best describe the EOFs, as they depict maximum and reduce towards the bottom measurements without crossing zero.

Comparison to previous studies

La Lama et al., 2016 suggested a similar conclusion, identifying a weaker decay depicted by the EOF derived from higher latitude regions, becoming non-zero at the last measurement. Noteworthy, the observation records obtained for this study do not reach the seabed, and a drastic decrease over the last meters could occur. However, this is unreasonable to assume as the total variance reveals a more substantial velocity at the lower measurements. Furthermore, the 'rough bottom' BC1 mode is typically accompanied by surface intensification, as the bottom relief alters the boundary condition, resulting in coupled horizontal and vertical velocities. As a result, the vertical mode becomes more surface intensified with weak horizontal flow at the bottom (LaCasce, 2017). However, as mentioned earlier, the investigated EOFs depict subsurface maximum, with a decrease towards shallower depth.

La Lama et al., 2016 further suggested the slow decay depicted by the EOFs could be related to the weak stratification in the Arctic. The EOFs and the analytical 'rough bottom' BC1 mode investigated by de La Lama differed first at greater depth, where the stratification became uniform with depth. In agreement with this suggestion, some EOFs analyzed in this study may resemble the 'rough bottom' BC1 mode, derived with uniform stratification, illustrated by LaCasce, 2017. The uniform 'rough bottom' BC1 mode reveals a smooth decay from the surface, fitting to the analyzed EOFs, only with a damped signal towards the top measurements. However, the comparable stations are shallow and resemble the deeper station in the same region for the equivalent depth. Therefore, because the deeper stations do not agree with the uniform 'rough bottom' BC1, it is possible the shallow stations only capture parts of the vertical structure and, again, are not representative of the Arctic. Nevertheless, the density is derived for the stations containing temperature and salinity measurements. The density may be interpreted as linear decaying for some of the stations. However, this is not significant and difficult to establish. Thus, conclusions regarding a correlation between the stratification and the EOFs can not be accomplished.

Suppose the 'rough bottom' BC mode best captures the vertical structure. In that case, topographic waves are expected to emerge as the 'rough bottom' boundary conditions switch the BT mode present with a 'flat bottom' to a topographic wave (Lacasce and Groeskamp, 2020). Topographic waves arise from the conservation of potential vorticity for water columns stretching/squashing due to sloping topography at the seabed. Thus, topographic waves are anticipated for horizontal flow over steep terrains, such as continental slopes. However, as the EOFs decrease towards the bottom and thus are not bottom intensified, no such signals are found in either the observation records or the model data.

The EOFs derived from the Lofoten stations are the only stations complying with the previous expectations for 'flat' and 'rough' bottom boundaries conditions. The stations reveal non-vanishing EOF for the basin mooring (MB) over 'flat' terrain, and weak or approximately vanishing EOF for the station over the slope. A comparison between the flat and sloping bottom in the Lofoten region performed by Isachsen, 2015 found the incline to reduce the growth rate and length scale of baroclinic eddies, resulting in vanishing amplitude at the bottom. However, changing the boundary condition to 'flat bottom' resulted in a non-vanishing amplitude. Thus, consistent with the findings in this thesis for the Lofoten region.

The two deeper stations in Lofoten, MB, and MW, depict the same subsurface peak between 400 to 600 meters. Trodahl, Isachsen et al., 2020 proposed eddies originate at varying depths in Lofoten in response to being subject to diverse cooling and warming periods during different seasons. The eddies are intensified over the slope and shed anticyclonic into the basin. Stacking effects reinforce the eddies, squeezing the denser eddy below the lighter one, which slides on top, becoming vertically aligned. Vertically alignment may explain the deeper maximum displayed in the EOFs for the MB and MW stations. However, if the theory were applicable, one may assume a second peak higher in the water column. Zhao and Timmermans, 2015 found similar evidence of vertical alignment in the Arctic Ocean, particularly in the Canadian Basin. Their findings indicated the deeper peak between approximately 300 to 500 meters, whereas the higher peak is above 200 meters.

Other wave theories

Waves arising from perturbations in the buoyancy frequency, N, and restored by gravity are called internal waves. Internal waves are not included in QG theory, as they propagate on considerably short timescales. The duration investigated is too short for the Rossby waves but too long for internal wave fluctuations. However, the vertical structure of Rossby and internal waves are similar, despite oscillating on quite different timescales. The structures investigated are neither Rossby nor internal waves, thus determining what sort of structures the EOFs capture remains.

Only stable modes have been discussed thus far. However, unstable modes are possible. Because the known stable modes agree with the EOFs insufficiently, the vertical structure observed in this study may reflect unstable waves. Nonlinear vortices have varied propagation properties as they advect PV with the ability to expand and shrink over time. Baroclinic instability can arise from releasing potential energy stored in sloping isopycnals. For the energy to be released, certain criteria must be satisfied. According to the Eady theory of instability, the horizontal buoyancy gradients must have the same sign at the top and bottom boundaries. The Eady theory does not consider internal PV gradients and thus has no β-effect, raising questions about how instability is altered. Internal PV gradients are taken into account by the Charney-Stern criteria and the Phillips model. Charney-Stern considers the same sign horizontal surface buoyancy gradient and interior PV gradients, or the opposite sign at the bottom, while Phillips considers opposite horizontal potential vorticity gradients in the interior (LaCasce, 2020). However, due to time limitations, these criteria are not considered further, and possible unstable flow can not be established. Nevertheless, several studies have found baroclinic instability to be a source of eddy activity in the Arctic interior (Meneghello et al., 2021, Wunsch, 1997, Zhao and Timmermans, 2015).

Model performance at observation site

Comparing the vertical structure at observation sites between the models' and the observations' EOFs revealed insufficient capability for the model to reproduce a comparable vertical structure. The model EOFs demonstrate weakly or zero signal at the bottom, whereas the observation EOFs have a substantial bottom response. The model validity at the surface is difficult to establish as the observation data lack measurements close to the surface. However, the observation EOFs reveals an unmistakable increase with depth from the top measurement. A comparable increase for the model EOFs is only visible for $EOF_{||}$ for the deeper stations North of Svalbard (E3, W3, and E2). Notably, W3 and E3 stations are the only two observation stations where the total variance illustrates an increase towards the surface, contradicting the observation EOFs. The opposed signal in the total variance indicates that the two stations may not have the same weak signal at the beginning as the other observation stations. Consequently, the W3 and E3 stations do not demonstrate the same signal as its corresponding observation EOF. The Yermak stations derived from model data illustrate EOFs increasing with depth from the surface, reaching a maximum at approximately mid-depth. Nevertheless, the observation EOF depicts a maximum close to the surface and the top measurement, decreasing below. Thus, the two EOFs are, again, not comparable. The deeper maximum in the model EOF repeats for several stations. The stations North of Svalbard, Yermak, and Beaufort illustrate a deeper maximum, whereas Lofoten and Barents show a maximum at the surface, decaying smoothly below. All deeper observation EOFs depict a maximum at a shallower depth.

The primary EOF for the model stations mainly resembles the 'rough bottom' BC1 mode, as the EOFs become weak or vanish at the bottom without crossing zero. Again, the exception is North of Svalbard and the basin station in Lofoten. The two deeper West stations North of Svalbard stations (W3 and W2) demonstrate one zero-crossing at shallower depths. One station displays vanishing EOFs at the bottom. Thus the second baroclinic 'rough bottom' mode may reflect the structure best, whereas, for the other, the 'flat bottom' BC1 may be more precise. The MB station in Lofoten reveals a more uniform decay, with non-vanishing EOFs at the bottom. Thus in agreement with the observation.

The model EOFs on continental slopes correspond with expectations and demonstrate $EOF_{||} > EOF_{\perp}$. However, comparison with observation may indicate that the model overperforms topographic steering. Several observation stations demonstrate isotropy, whereas the corresponding model station demonstrated anisotropy for the horizontal variance ellipses. The model drastically underperformed the velocity strength at all stations, except the Lofoten stations. The Lofoten area is the only observation region not experiencing sea ice. Sea ice cover is suggested to dampen eddy activity at the surface. Nevertheless, eddies are ubiquitous in the interior (Timmermans and Marshall, 2020), and thus, the sea ice cover can not explain the weak velocity performed by the model in these regions.

Notably, the total variance estimated with depth reveals an unrealistic high value for many stations. Both the model and observation data are derived using the exact procedure. Thus, the reason for the model data's misleading results for the total variance is uncertain and suspicious. However, the total variance is not removed as the structure is believed to be correct, and only the magnitude is misguiding.

Model performance on the effect of sea-ice and sloping/rough bottom topography

The EOFs derived from model data solemnly illustrate a substantially larger velocity for stations in ice-free areas compared to ice-covered regions. Nevertheless, these stations are located along the continental slope of Norway, where the Norwegian Current is expected. The exception is the EOF derived from South of Jan Mayen (ice-free region), illustrating weak velocities. The model does not display a dampened EOF signal towards the surface in areas covered by sea ice, except for the EOFs derived from the Laptev Sea. Here, the $EOF_{||}$ depicts a decrease from the last 100 meters towards the surface, increasing again right at the top. This structure is comparable to the dampening effect of sea ice suggested by Meneghello et al., 2021 on the unstable surface mode. None of the other model stations demonstrate a similar response.

The Makarov Basin and Bering Sea stations depict similar structures for the EOFs despite being derived from different depths. The two stations, located over flat or rough bottom, reveal equal strength and structure for the 160 meters they overlap. Both stations become weak below 100 meters depth, with $EOF_{||} = EOF_{\perp}$. Deep flow suppression from roughness is believed to be responsible for the EOFs vanishing/becoming weak at depth.

5.2 Further research

The Arctic region is particularly sensitive to environmental changes in a changing climate, with the ocean as a focal point. Therefore, enhanced knowledge about the geophysical dynamical processes ongoing in the ocean is necessary to understand further how these mechanisms alter Arctic warming (Timmermans and Marshall, 2020). As a master thesis is limited to time restrictions and, in this case lacking adequate data, the needs for further work are many.

This thesis aimed to characterize the Arctic ocean's vertical structure to identify a comparative analytical mode applying to the whole region. However, Rossby waves become marginal at higher latitude as β approaches zero at 90 degrees North. This results in long oscillation for Rossby waves in higher latitudes, extending over years in the Arctic, whereas the current meter records usually capture only one year of fluctuations. Thus, the timescale is too brief to investigate the duration of baroclinic Rossby waves in the Arctic region. Additionally, the nineteen records obtained for this thesis are insufficient for statistical significance. Hence, the necessity for a further survey of the Arctic Ocean is crucial.

The numerical ocean models have difficulties producing accurate simulations in the Arctic in response to the small deformation radius (Lacasce and Groeskamp, 2020). Thus, enhanced models' accuracy is essential for applying numerical models as compensation for unsatisfying observation records.

Lacasce and Groeskamp, 2020 suggests bottom roughness as a promising reason for deep flow suppression. However, the observation stations indicated non-vanishing EOFs at the bottom, unlike results from lower latitudes. Thus, questions regarding mechanisms preserving the flow in higher latitudes arise and further investigations are needed.

The observation records lack measurements for the surface and mix-layer. Thus, a complete examination of the entire structure is yet not feasible. However, LaCasce and Wang, 2015 found the mixed layer to have little effect on the structure below the layer itself. Thus, the dominant EOF obtained in this study is likely to be conserved, and it is only information on the surface layers lacking from the solution.

5.3 Conclusion

This study aimed to characterize the vertical structure of current fluctuation at higher latitudes. The observation records analyzed reveal non-vanishing velocity at the bottom measurements and deeper maximums than expected. Hence, the 'rough bottom' BC1 mode is inadequate in capturing the current fluctuations at higher latitude, as most of the EOFs analyzed in this study illustrate non-vanishing bottom velocity. However, the classic 'flat bottom' BC1 mode might be more insufficient, as only one EOF exhibit zero-crossings. Seventeen stations displayed a decay in the EOFs towards the top measurement, indicating reduced variance at a shallower depth. The two remaining stations with an opposite trend lack a considerable fraction of the surface information. The variance is expected to further increase towards shallower depth for the considered stations. The deeper mooring stations depict a subsurface maximum close to the first measurement. The moorings deployed in Lofoten support initial expectations for flow over steep and flat topography. Only the basin station revealed non-vanishing EOF at the bottom and isotropic variance. The remaining stations from Lofoten demonstrated EOFs vanishing or close to zero at the bottom, with a considerable percentage of the currents parallel to the incline.

So, in conclusion, as the EOFs mostly depict non-uniform, deep surface modes without zero-crossing, the 'rough bottom' BC1 mode may still be the preferred description of the vertical structure in higher latitudes. However, some stations reveal conflicting structures and are insufficiently captured by a singular mode, as the MB station located in Lofoten.

Topographic waves are predicted to emerge for the 'rough bottom' BC1 mode as the preferred analytical mode. The 'rough bottom' boundary condition substitutes the barotropic signal with a topographic wave response. However, none of the observation EOFs show evidence of topographic waves, as bottom intensification is not displayed.

Most of the mooring stations applied for this thesis are deployed over sloping topography. Thus, initial expectations were anisotropic variance ellipses orientated along the continental slope. However, the findings reveal mostly isotropic variance ellipses for the horizontal fluctuations. This trend is also visible in the EOFs, demonstrating an approximately equal fraction of fluctuations along and across the principal direction of variability obtained from horizontal EOF analysis applied for rotation. Only stations over profound slopes revealed asymmetric distribution in the current fluctuations.

Appendices

APPENDIX A

Figures and Tables

A.1 Figures

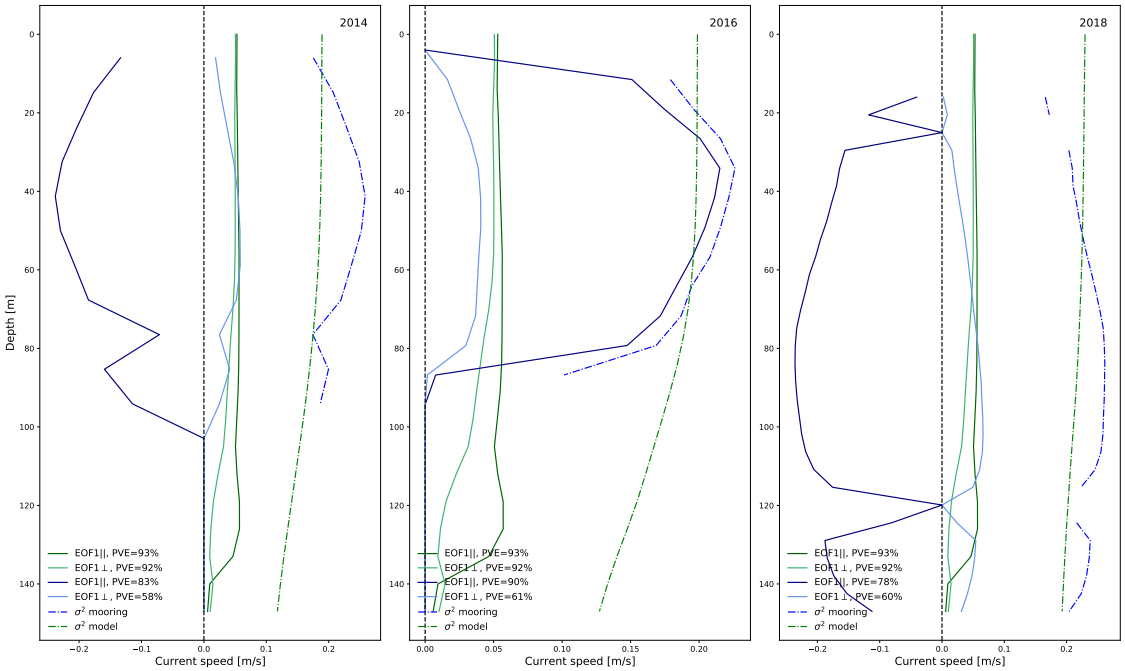

Figure A.1: EOF1 (solid line) and the total variance with depth (stippled with dots line) derived from model and observation data obtained from the Beaufort Sea. The model EOFs and total variance estimated with depth are visualized in green colors, whereas the observation EOFs and total variance estimated with depth are visualized in blue colors. Both model and observation EOFs are rotated along and across EOF1 derived from the horizontal velocities for each station. The 2014 mooring is visualized to the left, the 2016 mooring in the middle, and the 2018 mooring to the right.

A.2 Tables

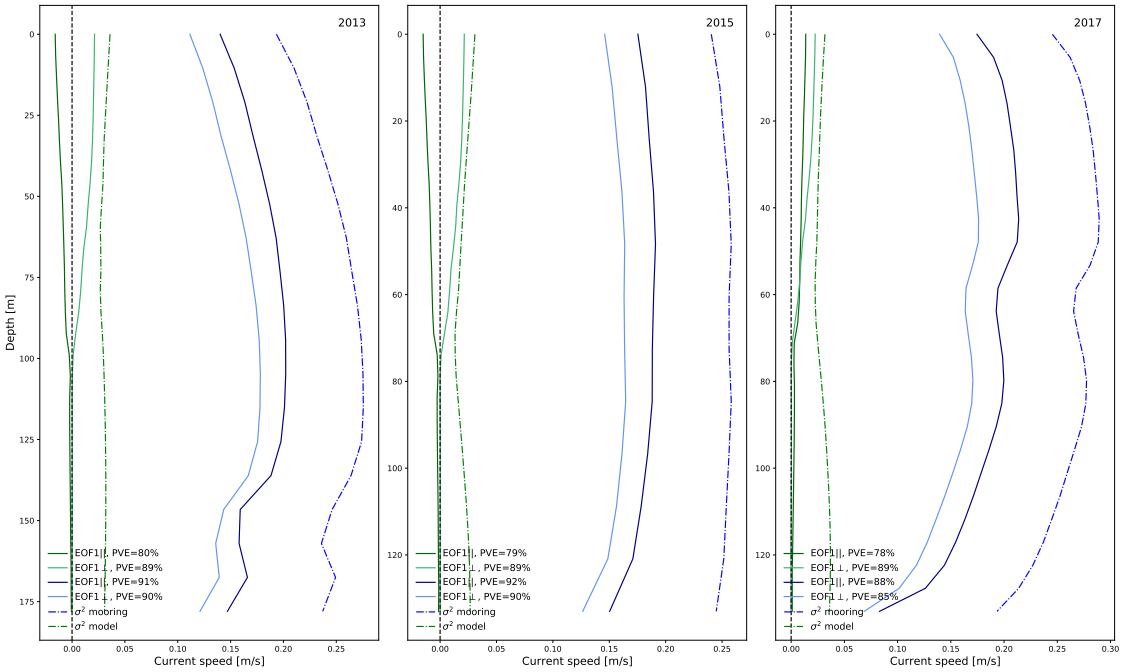

Figure A.2: EOF1 (solid line) and the total variance with depth (stippled with dots line) derived from model and observation data obtained from the Barents Sea. The model EOFs and total variance estimated with depth are visualized in green colors, whereas the observation EOFs and total variance estimated with depth are visualized in blue colors. Both model and observation EOFs are rotated along and across EOF1 derived from the horizontal velocities for each station. The deeper 2013 mooring is visualized to the left, the 2015 mooring in the middle, and the 2017 mooring to the right.

APPENDIX B

Computer Code

The python script produced for this study can be found following the link:

https://github.com/kaje2301/Master_2022

APPENDIX C

Equations

C.1 β-approximation

The momentum equation and the Coriolis term, f, are evaluated in different coordinate systems, where the momentum equation is in Cartesian coordinates, and the Coriolis term is in spherical coordinates. Thus, the Coriolis parameter is linearized for a given latitude, θ, to evaluate them in the same system. Taylor-expanding f around θ obtains

$$f(\theta) = f(\theta_0) + \frac{df}{d\theta}\theta_0(\theta - \theta_0) + \frac{1}{2}\frac{d^2f}{d^2\theta}\theta_0(\theta - \theta_0)^2 + ...$$

The range of latitude is limited thus all higher-order terms become small, and we can rewrite the equation to

$$f = f_0 + \beta y \tag{C.1}$$

where f_0 is the Coriolis parameter at θ_0, defined as

$$f = 2\Omega sin(\theta_0) \quad and \quad \beta = \frac{1}{R_e}\frac{df}{d\theta}(\theta_0) = \frac{2\omega}{R_e}cos(\theta),$$

R_e is the Earth's radius, and βy is the second term in the Taylor expansion. The β-approximation is then valid for

$$\frac{\beta L}{f_0} << 1,$$

thus length scale smaller than the radius of the Earth. The validity of the β-approximation varies with latitude, as it becomes more restricted as β approaches zero at 90 Degree North. The approximation is generally valid for a domain of up to a few thousand kilometers in N-S extent.

C.2 QG-Density equation

For baroclinic flow, the geostrophic velocity u_g, v_g varies with depth, so there is a need for a second equation, additionally to the depth-integrated Baroclinic-QGPV, to close the system. To solve this, we introduce the thermodynamic equation for the ocean:

$$\frac{d\rho}{dt} = \frac{\partial\rho}{\partial t} + \overline{u} \cdot \bigtriangledown\rho = 0 \tag{C.2}$$

Furthermore, are the density and pressure decomposed into perturbations and averaged parts, so we get:

$$\rho = \rho_0(z) + \rho'(x, y, z, t) \quad and \quad P = P_0(z) + P'(x, y, z, t)$$

where

$$|\rho| << \rho_0 \quad and \quad |P| << P_0,$$

so

$$\frac{\partial}{\partial z} P_0 = -\rho_0 g \quad and \quad \frac{\partial}{\partial z} P' = -\rho' g$$

.

By inserting the decomposed variables into the density equation, while neglecting vertical advection of perturbation compared to the averaged flow, and including the hydrostatic balance,

$$\frac{\partial P_0}{\partial z} = -\rho_0 g, \tag{C.3}$$

divided by -g, yields the quasi geostrophic density equation:

$$(\frac{\partial}{\partial t} - \frac{\partial \psi}{\partial y}\frac{\partial}{\partial x} + \frac{\partial \psi}{\partial x}\frac{\partial}{\partial y})\frac{\partial \psi}{\partial z} + \frac{N^2}{f_0} w = 0. \tag{C.4}$$

Bibliography

Analysis tools and methods (n.d.).

Armitage, T. (May 2016). 'Studies of the Arctic Ocean from satellite radar altimetry'. PhD thesis.

Baker-Yeboah, S., Watts, D. R. and Byrne, D. A. (2009). 'Measurements of Sea Surface Height Variability in the Eastern South Atlantic from Pressure Sensor–Equipped Inverted Echo Sounders: Baroclinic and Barotropic Components'. In: *Journal of Atmospheric and Oceanic Technology* vol. 26, no. 12, pp. 2593–2609.

De Mey, P. and Robinson, A. R. (1987). 'Assimilation of Altimeter Eddy Fields in a Limited-Area Quasi-Geostrophic Model'. In: *Journal of Physical Oceanography* vol. 17, no. 12, pp. 2280–2293.

Dupont, F., Higginson, S., Bourdalle-Badie, R., Lu, Y., Roy, F., Smith, G. C., Lemieux, J.-F., Garric, G. and Davidson, F. (2015). 'A high-resolution ocean and sea-ice modelling system for the Arctic and North Atlantic oceans'. In: *Geoscientific Model Development* vol. 8, no. 5, pp. 1577–1594.

Fer, I. (2020). 'Physical oceanography data from moorings in the Lofoten Basin, Norwegian Sea: June 2016 – September 2017'. In.

Fer, I. and Peterson, A. K. (2019). 'Moored measurements of ocean current, temperature and salinity from Yermak Plateau, Sep. 2014 - Aug. 2015'. In.

Gurvan, M. et al. (Oct. 2017). 'NEMO ocean engine'. In: *Notes du Pôle de modélisation de lÍnstitut Pierre-Simon Laplace (IPSL)*, no. 27. Revision 8625 from SVN repository (missing links).

Held, I. M., Pierrehumbert, R. T., Garner Stephen, T. and Swanson, K. L. (1995). 'Surface quasi-geostrophic dynamics'. In: *Journal of Fluid Mechanics* vol. 282, pp. 1–20.

Ilker, F. (2022). *Metadata for moorings North of Svalbard*.

Isachsen, P. E. (2015). 'Baroclinic instability and the mesoscale eddy field around the Lofoten Basin'. In: *Journal of Geophysical Research: Oceans* vol. 120, no. 4, pp. 2884–2903.

Isern-Fontanet, J., Chapron, B., Lapeyre, G. and P., K. (May 2006). 'Potential use of microwave sea surface temperatures for the estimation of ocean currents.' In: *Geophysical Research Letters* vol. 33, p. L24608.

La Lama, M. S. de, LaCasce, J. H. and Fuhr, H. K. (Sept. 2016). 'The vertical structure of ocean eddies'. In: *Dynamics and Statistics of the Climate System* vol. 1. dzw001.

LaCasce, J. H. (2017). 'The Prevalence of Oceanic Surface Modes'. In: *Geophysical Research Letters* vol. 44, no. 21, pp. 11, 097–11, 105.

— (2020). *Atmosphere-Ocean Dynamics*. Oslo, Norway: Department of Geosciences, University of Oslo.

Lacasce, J. H. and Groeskamp, S. (Aug. 2020). 'Baroclinic Modes over Rough Bathymetry and the Surface Deformation Radius'. In: *Journal of Physical Oceanography* vol. 50, pp. 1–40.

LaCasce, J. H. and Mahadevan, A. (Sept. 2006). 'Estimating subsurface horizontal and vertical velocities from sea-surface temperature'. In: *Journal of Marine Research* vol. 64, pp. 695–721.

LaCasce, J. H. and Wang, J. (July 2015). 'Estimating Subsurface Velocities from Surface Fields with Idealized Stratification'. In: *Journal of Physical Oceanography* vol. 45, no. 9, pp. 2424–2435.

Lapeyre, G. (Sept. 2009). 'What Vertical Mode Does the Altimeter Reflect? On the Decomposition in Baroclinic Modes and on a Surface-Trapped Mode'. In: *Journal of Physical Oceanography* vol. 39, no. 11, pp. 2857–2874.

Lapeyre, G. and Klein, P. (Feb. 2006). 'Dynamics of the Upper Oceanic Layers in Terms of Surface Quasigeostrophy Theory'. In: *Journal of Physical Oceanography* vol. 36, no. 2, pp. 165–176.

Meneghello, G., Marshall, J., Lique, C., Isachsen, P. E., Doddridge, E., Campin, J.-M., Regan, H. and Talandier, C. (2021). 'Genesis and Decay of Mesoscale Baroclinic Eddies in the Seasonally Ice-Covered Interior Arctic Ocean'. In: *Journal of Physical Oceanography* vol. 51, no. 1, pp. 115–129.

Nummelin, A., Li, C. and Smedsrud, L. H. (2015). 'Response of Arctic Ocean stratification to changing river runoff in a column model'. In: *Journal of Geophysical Research: Oceans* vol. 120, no. 4, pp. 2655–2675.

Overland, J., Dunlea, E., Box, J. E., Corell, R., Forsius, M., Kattsov, V., Olsen, M. S., Pawlak, J., Reiersen, L.-O. and Wang, M. (2019). 'The urgency of Arctic change'. In: *Polar Science* vol. 21. ISAR-5/ Fifth International Symposium on Arctic Research, pp. 6–13.

Robert S. Pickart, P. I. (2020). *A mooring in the western Arctic boundary current.*

Rudels, B., LarssonAnne-Marie and SehlstedtPer-Ingvar (Jan. 1991). 'Stratification and water mass formation in the Arctic Ocean: some implications for the nutrient distribution'. In: *Polar Research* vol. 10, no. 1, pp. 19–32.

Stammer, D. (1997). 'Global Characteristics of Ocean Variability Estimated from Regional TOPEX/POSEIDON Altimeter Measurements'. In: *Journal of Physical Oceanography* vol. 27, no. 8, pp. 1743–1769.

Sundfjord, A. (2021). *Long-term variability and trends in the Atlantic Water inflow region (A-TWAIN).*

Timmermans, M.-L. and Marshall, J. (2020). 'Understanding Arctic Ocean Circulation: A Review of Ocean Dynamics in a Changing Climate'. In: *Journal of Geophysical Research: Oceans* vol. 125, no. 4. e2018JC014378 10.1029/2018JC014378, e2018JC014378.

Trodahl, M. and Isachsen, P. E. (2018). 'Topographic Influence on Baroclinic Instability and the Mesoscale Eddy Field in the Northern North Atlantic Ocean and the Nordic Seas'. In: *Journal of Physical Oceanography* vol. 48, no. 11, pp. 2593–2607.

Trodahl, M., Isachsen, P. E., Lilly, J. M., Nilsson, J. and Kristensen, N. M. (2020). 'The Regeneration of the Lofoten Vortex through Vertical Alignment'. In: *Journal of Physical Oceanography* vol. 50, no. 9, pp. 2689–2711.

Tulloch, R. and Smith, K. S. (Sept. 2006). 'A theory for the atmospheric energy spectrum: Depth-limited temperature anomalies at the tropopause'. In: *Proc Natl Acad Sci U S A* vol. 130, no. 40, pp. 14690–14694.

Vallis, G. K. (2017). *Atmospheric and Oceanic Fluid Dynamics: Fundamentals and Large-Scale Circulation*. 2nd ed. Cambridge: Cambridge University Press.

Wang, J., Flierl, G. R., LaCasce, J. H., McClean, J. L. and Mahadevan, A. (Aug. 2013). 'Reconstructing the Ocean's Interior from Surface Data'. In: *Journal of Physical Oceanography* vol. 43, pp. 1611–1625.

Wunsch, C. (1997). 'The Vertical Partition of Oceanic Horizontal Kinetic Energy'. In: *Journal of Physical Oceanography* vol. 27, no. 8, pp. 1770–1794.

Wunsch, C. and Stammer, D. (1995). 'The global frequency-wavenumber spectrum of oceanic variability estimated from TOPEX/POSEIDON altimetric measurements'. In: *Journal of Geophysical Research: Oceans* vol. 100, no. C12, pp. 24895–24910. eprint: https://agupubs.onlinelibrary.wiley.com/doi/pdf/10.1029/95JC01783.

Zhao, M. and Timmermans, M.-L. (2015). 'Vertical scales and dynamics of eddies in the Arctic Ocean's Canada Basin'. In: *Journal of Geophysical Research: Oceans* vol. 120, no. 12, pp. 8195–8209.